

Methanol deuteration in high-mass protostars

M. L. van Gelder¹, J. Jaspers¹, P. Nazari¹, A. Ahmadi¹, E. F. van Dishoeck^{1,2}, M. T. Beltrán³,
G. A. Fuller^{4,5}, Á. Sánchez-Monge⁵, and P. Schilke⁵

¹ Leiden Observatory, Leiden University, PO Box 9513, 2300RA Leiden, The Netherlands
e-mail: v.gelder@strw.leidenuniv.nl

² Max Planck Institut für Extraterrestrische Physik (MPE), Giessenbachstrasse 1, 85748 Garching, Germany

³ INAF-Osservatorio Astrofisico di Arcetri, Largo E. Fermi 5, 50125 Firenze, Italy

⁴ Jodrell Bank Centre for Astrophysics, Department of Physics and Astronomy, University of Manchester, Oxford Road, Manchester, M13 9PL, UK

⁵ I. Physikalisches Institut, Universität zu Köln, Zùlpicher Str.77, 50937, Köln, Germany

Received XXX; accepted XXX

ABSTRACT

Context. The deuteration of molecules forming in the ices such as methanol (CH_3OH) is sensitive to the physical conditions during their formation in dense cold clouds and can be probed through observations of deuterated methanol in hot cores.

Aims. The aim is to determine the D/H ratio of methanol for a large sample of 99 high-mass protostars and to link this to the physical conditions during the formation of methanol in the prestellar phases.

Methods. Observations with the Atacama Large Millimeter/submillimeter Array (ALMA) containing transitions of CH_3OH , CH_2DOH , CHD_2OH , $^{13}\text{CH}_3\text{OH}$, and $\text{CH}_3^{18}\text{OH}$ are investigated. The column densities of CH_2DOH , CHD_2OH , and CH_3OH are determined for all sources, where the column density of CH_3OH is derived from optically thin ^{13}C and ^{18}O isotopologues. Consequently, the D/H ratio of methanol is derived taking statistical effects into account.

Results. Singly deuterated methanol (CH_2DOH) is detected at the 3σ level toward 25 of the 99 sources in our sample of the high-mass protostars. Including upper limits, the $(\text{D}/\text{H})_{\text{CH}_3\text{OH}}$ ratio inferred from $N_{\text{CH}_2\text{DOH}}/N_{\text{CH}_3\text{OH}}$ was derived for 38 of the 99 sources and varies between $\sim 10^{-3} - 10^{-2}$. Including other high-mass hot cores from the literature, the mean methanol D/H ratio is $1.1 \pm 0.7 \times 10^{-3}$. This is more than one order of magnitude lower than what is seen for low-mass protostellar systems ($2.2 \pm 1.2 \times 10^{-2}$). Doubly deuterated methanol (CHD_2OH) is detected at the 3σ level toward 11 of the 99 sources. Including upper limits for 15 sources, the $(\text{D}/\text{H})_{\text{CH}_2\text{DOH}}$ ratios derived from $N_{\text{CHD}_2\text{OH}}/N_{\text{CH}_2\text{DOH}}$ are more than two orders of magnitude higher than $(\text{D}/\text{H})_{\text{CH}_3\text{OH}}$ with an average of $2.0 \pm 0.8 \times 10^{-1}$ which is similar to what is found for low-mass sources. Comparison with literature GRAINOBLE models suggests that the high-mass prestellar phases are either warm (> 20 K) or live shorter than the free-fall timescale. In contrast, for low-mass protostars, both a low temperature of < 15 K and a prestellar phase timescale longer than the free-fall timescale are necessary.

Conclusions. The $(\text{D}/\text{H})_{\text{CH}_3\text{OH}}$ ratio drops by more than an order of magnitude between low-mass and high-mass protostars due to either a higher temperature during the prestellar phases or shorter prestellar phases. However, successive deuteration toward CHD_2OH seems equally effective between low-mass and high-mass systems.

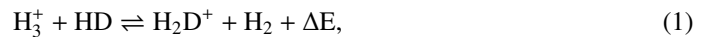
Key words. astrochemistry – stars: formation – stars: protostars – techniques: interferometric – ISM: molecules

1. Introduction

Isotopologues have proven to be vital in our understanding of the star and planet formation process. They allow for studying the most abundant species for which the emission originating from the main isotopologue is optically thick. Moreover, the sensitivity of isotopologue ratios to the physical conditions such as temperature and ultraviolet (UV) radiation has proven key in understanding the molecular journey during the entire star formation process (see e.g., reviews by Caselli & Ceccarelli 2012; Tielens 2013; Ceccarelli et al. 2014). One of the most studied isotopologues are those that contain deuterium (D). These deuterated molecules are suggested to form already in the cold prestellar phases (e.g., van Dishoeck et al. 1995; Caselli & Ceccarelli 2012; Ceccarelli et al. 2014). Especially for molecules such as methanol (CH_3OH) that form on the surfaces of dust grains in dense cores, D/H fractionation ratios up to 10% are found toward low-mass protostars (e.g., Bianchi et al. 2017a,b; Taquet et al. 2019; van Gelder et al. 2020), more than four orders of magnitude larger than the canonical D/H ratio derived for the

local interstellar medium (ISM) of $\sim 2 \times 10^{-5}$ (Linsky et al. 2006; Prodanović et al. 2010). It is thus key to understand the deuterium fractionation process in the earliest phases of star formation.

The gaseous atomic D/H ratio can be increased in the prestellar phases through the exothermic reaction (Watson 1974; Aikawa & Herbst 1999; Ceccarelli et al. 2014),



where $\Delta E = 232$ K. Since in the cold ($\lesssim 20$ K) prestellar cores the backward reaction in Eq. (1) is less efficient, H_2D^+ is enhanced and the atomic D/H ratio in the gas phase can be effectively increased through dissociative recombination of H_2D^+ with free electrons. Moreover, gaseous CO is the main destructor of H_3^+ and H_2D^+ (Brown & Millar 1989; Roberts et al. 2003) and thus the heavy CO freeze-out in dense ($\gtrsim 10^4 \text{ cm}^{-3}$) prestellar cores additionally stimulates the increase of the gaseous atomic D/H ratio. In turn, the enhanced atomic D/H ratio in the gas can translate into a higher D/H ratio of molecules forming in the ices

(Tielens 1983; Nagaoka et al. 2005). Measuring the deuteration of molecules that form in the ices is thus a powerful tool to determine the physical conditions such as density (e.g., CO freeze-out) and temperature during their formation.

Methanol forms on the surfaces of dust grains in dense prestellar phases through the hydrogenation of CO ice (e.g., Watanabe & Kouchi 2002; Fuchs et al. 2009) and reactions between its grains-surface products (e.g., H_2CO and CH_3O Simons et al. 2020; Santos et al. 2022) and is therefore expected to exhibit a high D/H ratio. This is in strong contrast to, for example, water for which the bulk of the ice is formed in the warmer translucent cloud phase leading to a rather low overall $\text{HDO}/\text{H}_2\text{O}$ ratio ($\lesssim 0.1\%$; Persson et al. 2014; Furuya et al. 2016; Jensen et al. 2019; van't Hoff et al. 2022). The sensitivity of the methanol deuteration process to temperature was investigated by Bøgelund et al. (2018) using the GRAINOBLE gas-grain chemical model (Taquet et al. 2012, 2013, 2014), finding a strong correlation between the D/H ratio of methanol and the formation temperature. Moreover, Taquet et al. (2019) showed that the timescale of the prestellar phase is highly relevant for methanol deuteration.

Methanol and its (deuterated) isotopologues are readily observed as they desorb from the dust grains. Mono deuterated methanol, CH_2DOH and CH_3OD , have been observed in the warm inner regions of both low-mass and high-mass protostellar systems (e.g., Fuente et al. 2014; Belloche et al. 2016; Bøgelund et al. 2018; van Gelder et al. 2020; van der Walt et al. 2021). Similarly, both doubly and triply deuterated methanol have been detected in hot cores (e.g., Parise et al. 2002, 2004; Bianchi et al. 2017a; Drozdovskaya et al. 2022; Ilyushin et al. 2022). Moreover, CH_2DOH has also been detected in both low-mass prestellar cores (e.g., Bizzocchi et al. 2014; Lattanzi et al. 2020; Ambrose et al. 2021) and high-mass starless cores (e.g., Fontani et al. 2015). Across this mass and evolutionary range, the D/H ratio of singly deuterated methanol varies orders of magnitude. The D/H ratio is on the order of 10% for low-mass prestellar cores, low-mass protostars, and comets (e.g., Bianchi et al. 2017a,b; Jørgensen et al. 2018; Taquet et al. 2019; Manigand et al. 2020; van Gelder et al. 2020; Lattanzi et al. 2020; Ambrose et al. 2021; Drozdovskaya et al. 2021). Interestingly, successive deuteration toward CHD_2OH and CD_3OH seems to be quite effective in low-mass protostars (about 15–25%; Drozdovskaya et al. 2022; Ilyushin et al. 2022). On the other hand, the D/H ratio derived from CH_2DOH is as low as 0.1 – 0.01% for high-mass starless cores and high-mass protostars (Fontani et al. 2015; Neill et al. 2013; Belloche et al. 2016; Bøgelund et al. 2018). However, the sample of high-mass protostars for which reliable and interferometrically derived methanol D/H ratios are available (e.g., Orion KL, Sgr B2(N2), NGC 6334I) remains small compared to the low-mass sources (~ 20 sources). Furthermore, no interferometric detections of CHD_2OH in high-mass sources have been presented thus far.

In this work, the methanol D/H ratios are derived for an additional 99 high-mass sources based on ALMA observations of CH_2DOH , CHD_2OH , CH_3OH , $^{13}\text{CH}_3\text{OH}$, $\text{CH}_3^{18}\text{OH}$. In Sect. 2, the observations and derivation of the column densities are explained. The resulting D/H ratios of CH_3OH and CH_2DOH are presented in Sect. 3. In Sect. 4, the methanol D/H ratios derived for our high-mass sources are compared to their low-mass counterparts and prestellar phases. Furthermore, through comparison with the GRAINOBLE models computed by Bøgelund et al. (2018) and Taquet et al. (2019), the effect of physical conditions on the methanol D/H ratio is discussed. Our main conclusions are listed in Sect. 5.

2. Methodology

2.1. Observations

The dataset analyzed in this work was taken from the ALMA Evolutionary study of High Mass Protocluster Formation in the Galaxy (ALMAGAL) survey (2019.1.00195.L; PI: S. Molinari) that targeted over 1000 dense clumps with $M > 500 M_\odot$ based on the *Herschel* Hi-Gal survey (Molinari et al. 2010; Elia et al. 2017, 2021). The ALMAGAL survey covers frequencies from ~ 217 GHz to ~ 221 GHz with multiple configurations of ALMA down to $\sim 0.1''$ resolution at a spectral resolution of between $\sim 0.2 - 0.7 \text{ km s}^{-1}$. In this work a subsample of 40 high-mass cores is selected based on high bolometric luminosity ($L_{\text{bol}} > 1000 L_\odot$) and the sources being rich in lines from complex organic molecules (COMs) such as CH_3OH and CH_3CN . Only archival data with a beam smaller than $2''$ ($\sim 1000 - 5000 \text{ au}$) that were public before February 2021 are included. This selection introduces a bias in our sample to line-rich sources and means that not all high-mass cores in the ALMAGAL survey are covered. In the higher resolution ALMA data, the 40 Hi-Gal high-mass cores are resolved into in total 99 sources based on the continuum emission (labeled A, B, C, etc., see Appendix B). These 99 sources are all studied in this work and are the same as those that were analyzed by van Gelder et al. (2022). The data are pipeline calibrated and imaged with the Common Astronomy Software Applications¹ (CASA; McMullin et al. 2007) version 5.6.1. The angular resolution of the data ranges from $0.5 - 1.25''$, corresponding to about $\sim 2500 - 10000 \text{ au}$ at the range of distances covered ($2 - 12 \text{ kpc}$; Mège et al. 2021), and the data have a sensitivity of $\sim 0.2 \text{ K}$. The ALMAGAL data cover several transitions of CH_3OH , four transitions of $^{13}\text{CH}_3\text{OH}$, nine transitions of $\text{CH}_3^{18}\text{OH}$, 21 transitions of CH_2DOH , and 22 transitions of CHD_2OH (see Appendix A). Also nine transitions of CD_3OH are covered (Ilyushin et al. 2022), but these are not detected toward any of the sources. No transitions of CH_3OD are covered in the observed frequency range. Both CD_3OH and CH_3OD are therefore not analyzed further in this paper.

Integrated intensity maps of the $\text{CH}_3\text{OH } 8_{0,8} - 7_{1,6}$, $\text{CH}_2\text{DOH } 17_{1,16} e_0 - 17_{0,17} e_0$, and $\text{CHD}_2\text{OH } 7_{0,1} e_1 - 6_{1,1} e_1$ lines for the source 881427 are presented in Fig. 1. The source 881427 hosts three nearby hot cores with varying line strengths and line widths and is a representative source of the rest of the sample. Whereas the emission of CH_3OH is often larger than the central beam, the emission of both CH_2DOH and CHD_2OH is generally confined within the central beam similar to the ^{13}C and ^{18}O isotopologues. The main exception for this is $\text{CH}_2\text{DOH } 5_{1,5} e_0 - 4_{1,4} e_0$ ($E_{\text{up}} = 36 \text{ K}$) which often shows more extended emission. This is likely because the low upper energy level of this line is also sensitive to cold ($T \lesssim 70 \text{ K}$) material where methanol is nonthermally desorbed from the grains (e.g., Perotti et al. 2020, 2021). To exclude the contribution of extended emission, this transition is not included in the analysis described below.

The spectra are extracted from the peak pixel in the $\text{CH}_3\text{OH } 8_{0,8} - 7_{1,6}$ ($E_{\text{up}} = 97 \text{ K}$) integrated intensity maps for all sources that show this at the $> 3\sigma$ level. This line is strongest transition of CH_3OH in the sample with $E_{\text{up}} > 70 \text{ K}$ (lines with lower E_{up} can suffer from contamination by the outflow or extended emission). For sources that do not show emission from the $\text{CH}_3\text{OH } 8_{0,8} - 7_{1,6}$ line, spectra are extracted from the peak continuum pixel and only upper limits on the column densities of CH_3OH (and isotopologues) are derived. In the G323.7399-00.2617B cluster, which contains seven nearby cores, all spec-

¹ <https://casa.nrao.edu/>

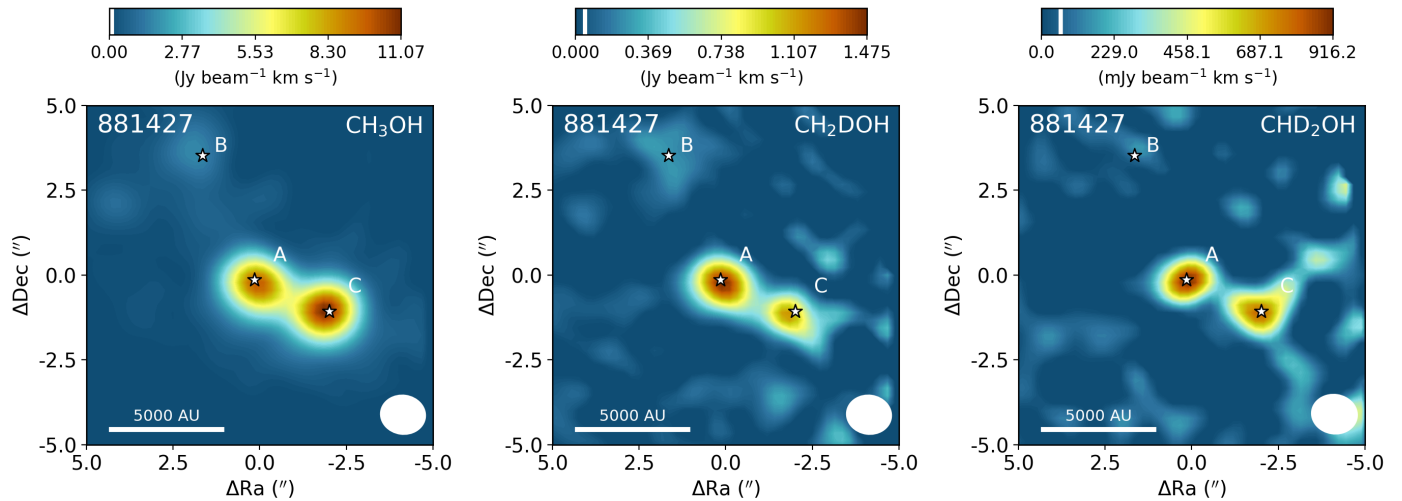


Fig. 1. Integrated intensity maps of the CH_3OH $8_{0,8} - 7_{1,6}$ ($E_{\text{up}} = 97$ K, left), CH_2DOH $17_{1,16} e_0 - 17_{0,17} e_0$ ($E_{\text{up}} = 336$ K, middle), and CHD_2OH $7_{0,1} e_1 - 6_{1,1} e_1$ ($E_{\text{up}} = 74$ K, right) lines for 881427. The color scale is shown on top of each image. The image is integrated over $[-5, 5] \text{ km s}^{-1}$ with respect to the V_{lsr} of source A. The white vertical line in the colorbar indicates the 3σ threshold. The source positions based on the continuum emission are indicated with the white stars. The white ellipse in the lower right of each image depicts the beam size and in the lower left a physical scale bar is displayed.

tra are extracted from the same positions as van Gelder et al. (2022). In G023.3891+00.1851, the emission of CH_2DOH peaks offset by about half the beam ($\sim 0.6''$) and therefore the spectrum is extracted from the peak of CH_2DOH $17_{1,16} e_0 - 17_{0,17} e_0$ ($E_{\text{up}} = 336$ K). For all other sources, the peak in CH_3OH coincides with the peaks of CH_2DOH and CHD_2OH . For sources also included by Nazari et al. (2022), our spectral extraction locations are the same as theirs, which are extracted from the peak position of the CH_3CN $12_4 - 11_4$ integrated intensity maps, except for 721992 and G023.3891+00.1851 where the CH_3OH $8_{0,8} - 7_{1,6}$ and CH_2DOH $17_{1,16} e_0 - 17_{0,17} e_0$ emission peaks offset from the CH_3CN $12_4 - 11_4$ emission by about $1''$. It is important to note that these spectral extraction positions are different by up to $1''$ from van Gelder et al. (2022) who extracted their spectra from the peak continuum pixel for all sources. Therefore, the column densities derived in this work may deviate from theirs. The reason why our spectra are extracted from the peak pixel of CH_3OH is to have the highest signal-to-noise in methanol lines and its isotopologues the extracted spectra.

2.2. Deriving the column densities

The column densities of all methanol isotopologues are derived using the spectral analysis tool CASSIS² (Vastel et al. 2015) under the assumption of local thermodynamic equilibrium (LTE). The line lists of CH_3OH , $^{13}\text{CH}_3\text{OH}$, and $\text{CH}_3^{18}\text{OH}$ are taken from the CDMS catalog³ (Müller et al. 2001, 2005; Endres et al. 2016). These entries include the first three (CH_3OH) and two ($^{13}\text{CH}_3\text{OH}$ and $\text{CH}_3^{18}\text{OH}$) torsional states and are based on the works of Xu et al. (2008), Xu & Lovas (1997), and Fisher et al. (2007), respectively. The difference between the statistical weight factors g_1 of $^{13}\text{CH}_3\text{OH}$ ($g_1 = 1$) and $\text{CH}_3^{18}\text{OH}$ and CH_3OH ($g_1 = 4$) is correctly taken into account in the CDMS database entries and therefore does not affect any column densities derived in this work. The line list of CH_2DOH is taken from the JPL catalog⁴ (Pickett et al. 1998), where the entry is based

on the work of Pearson et al. (2012). The line list of CHD_2OH is taken from Drozdovskaya et al. (2022), which is mostly based on the the work of Coudert et al. (2021).

Only transitions with $E_{\text{up}} \geq 50$ K are used to derive the column densities since lines with lower E_{up} likely include also emission from non-thermally desorbed methanol and emission possibly related to outflows. For $^{13}\text{CH}_3\text{OH}$, the $14_{1,13} - 13_{2,12}$ ($E_{\text{up}} = 254$ K) transition gives the only constraint on the column density for many sources as the other transitions suffer from severe line blending. Similarly, for $\text{CH}_3^{18}\text{OH}$ only the $8_{1,8} - 7_{0,7}$ ($E_{\text{up}} = 86$ K) and $14_{1,14} - 13_{2,12}$ ($E_{\text{up}} = 239$ K) transitions provide constraints on the column density as well as some information on the excitation temperature. Furthermore, for CH_2DOH the $5_{2,4} e_1 - 4_{1,5} e_1$ ($E_{\text{up}} = 59$ K) line, as well as several other lines, have rather low Einstein A_{ij} values ($< 10^{-5} \text{ s}^{-1}$) and are often blended with other COMs. Moreover, the spectroscopy of the CH_2DOH $18_{1,17} o_1 - 18_{2,17} e_0$ line is unreliable and shows large discrepancies in A_{ij} between the JPL catalog entry ($A_{ij} = 1.8 \times 10^{-5} \text{ s}^{-1}$) and that derived by Coudert et al. (2014, $A_{ij} = 8.9 \times 10^{-7} \text{ s}^{-1}$) and is therefore also excluded from the analysis. Consequently, the $17_{1,16} e_0 - 17_{0,17} e_0$ ($E_{\text{up}} = 336$ K) transition of CH_2DOH provided the best constraint on the column density of CH_2DOH . However, although the $5_{1,5} e_0 - 4_{1,4} e_0$ ($E_{\text{up}} = 36$ K) transition is excluded from the fitting, it can provide information on the excitation temperature of CH_2DOH as the best-fit LTE model should not overproduce this line. Lastly, for CHD_2OH , the $7_{0,1} e_1 - 6_{1,1} e_1$ ($E_{\text{up}} = 74$ K) transition is the only detected line in our sample and therefore is the only constraint on the column density of CHD_2OH .

As a consequence of only single or a few lines being available, the excitation temperature is fixed to 150 K, which is roughly the mean temperature as measured toward other high-mass hot cores (e.g., Neill et al. 2013; Belloche et al. 2016; Bøgelund et al. 2018, 2019). However, if clear anticorrelations between the best-fit LTE model and the data were present, the excitation temperature was varied by eye in steps of 25 K until the anticorrelations disappear in a similar way as the by eye fit method of Nazari et al. (2021, see their Appendix C).

² <http://cassis.irap.omp.eu/>

³ <https://cdms.astro.uni-koeln.de/>

⁴ <https://spec.jpl.nasa.gov/>

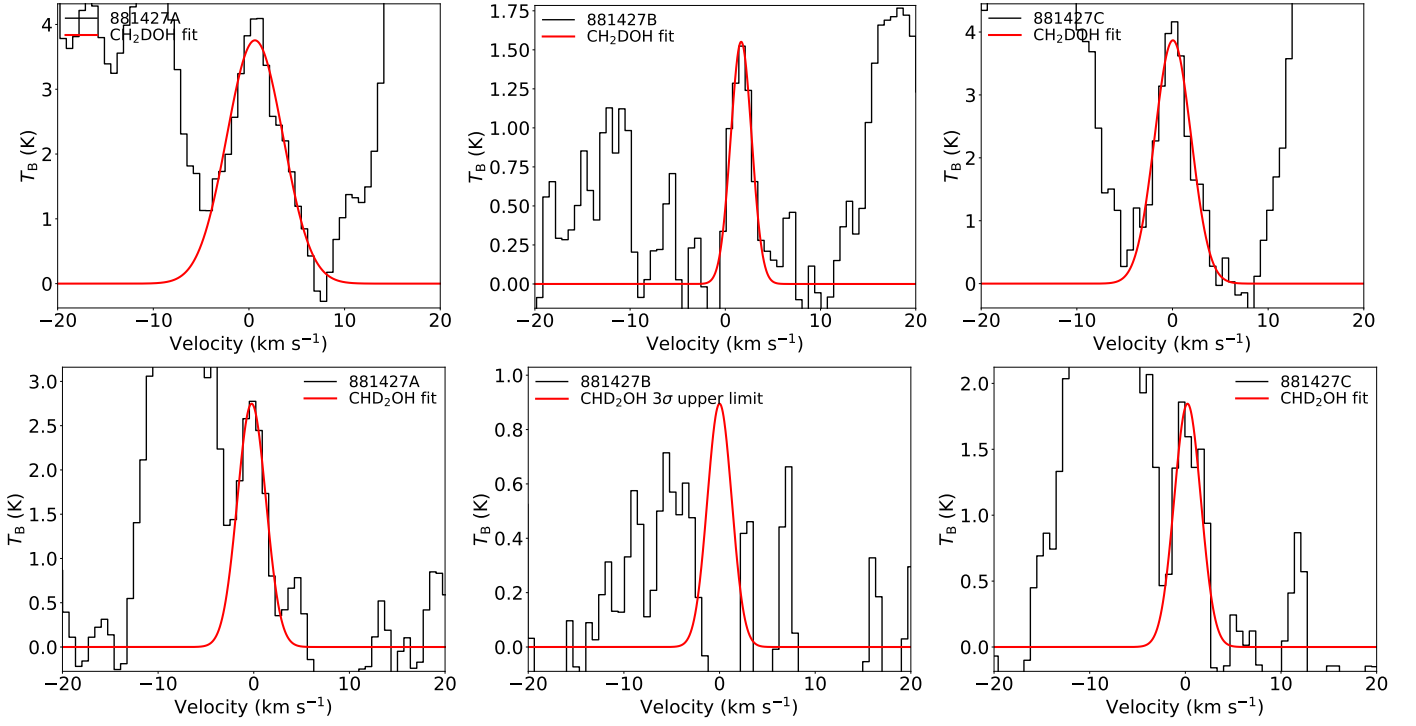


Fig. 2. Spectral line fits of $\text{CH}_2\text{DOH } 17_{1,16} e_0 - 17_{0,17} e_0$ ($E_{\text{up}} = 336$ K, top row) and $\text{CHD}_2\text{OH } 7_{0,1} e_1 - 6_{1,1} e_1$ ($E_{\text{up}} = 74$ K, bottom row) for 881427A (left), 881427B (middle), and 881427C (right). The data corrected for the V_{lsr} are shown in black and the best fit for $T_{\text{ex}} = 150$ K is shown in red.

The column densities N of $^{13}\text{CH}_3\text{OH}$, $\text{CH}_3^{18}\text{OH}$, CH_2DOH , and CHD_2OH are derived following a similar method as van Gelder et al. (2020). A grid of N and the full width at half maximum (FWHM) of the line is set and a model spectrum is computed for each grid point assuming LTE conditions. The size of the emitting region is fixed to the size of the beam (see Appendix B). Blended lines are excluded from the fitting procedure and similarly broad lines ($\text{FWHM} \geq 10$ km s $^{-1}$) and lines with $E_{\text{up}} \leq 50$ K are excluded in the fit to exclude any emission possibly related to outflows. The best-fit column density and the 2σ uncertainty are computed from the grid for each isotopologue. The main contributors to the uncertainty of N are the uncertainty on the flux calibration of ALMA (assumed to be 10%) and the assumed excitation temperature. However, changing the excitation temperature in the 100–300 K range leads to at most a factor 3 variation in the derived column densities. For several sources (e.g., 705768), the lines are broad (> 7 km s $^{-1}$) making automated line fitting complicated. For these sources the column density is estimated using the by eye fitting method of Nazari et al. (2021). In this case, a 50% uncertainty on the column density is assumed. Moreover, the sources 101899, 615590, 865468, and G345.5043+00.3480 showed line profiles consisting of multiple components. The column density of each component is derived and reported separately.

For all sources, the column density of CH_3OH is derived from $\text{CH}_3^{18}\text{OH}$ and, when no lines originating from $\text{CH}_3^{18}\text{OH}$ were detected, from $^{13}\text{CH}_3\text{OH}$. The adopted $^{12}\text{C}/^{13}\text{C}$ and $^{16}\text{O}/^{18}\text{O}$ ratios are dependent on the galactocentric distance and are determined using the relations of Milam et al. (2005) and Wilson & Rood (1994), respectively. In cases where only upper limits on the column densities of both $^{13}\text{CH}_3\text{OH}$ and $\text{CH}_3^{18}\text{OH}$ could be derived, the range in $N_{\text{CH}_3\text{OH}}$ was calculated by setting the 3σ upper limit based on scaling the 3σ upper limit of $^{13}\text{CH}_3\text{OH}$ and the lower limit based on the main isotopologue.

Lastly, when CH_3OH was not detected, the 3σ upper limit is derived directly from CH_3OH lines.

3. Results

The derived column densities of all isotopologues are presented in Table B.1 for the reported excitation temperature. In Fig. 2, the best-fit models to the $\text{CH}_2\text{DOH } 17_{1,16} e_0 - 17_{0,17} e_0$ and $\text{CHD}_2\text{OH } 7_{0,1} e_1 - 6_{1,1} e_1$ lines are presented for three hot cores in 881427 (see Fig. 1). Toward 25 sources, at least one clean unblended line of CH_2DOH is detected at the 3σ level, allowing for the determination of the column density. For the remaining 74 sources where no (unblended) transitions of CH_2DOH are detected, the 3σ upper limit is reported. For CHD_2OH , the column density could be determined for 11 sources. In Table B.1, the column densities of $^{13}\text{CH}_3\text{OH}$, $\text{CH}_3^{18}\text{OH}$, and CH_3OH are also reported.

The column densities of CH_2DOH are generally between one and three orders of magnitude lower than those of CH_3OH , see also Fig. 3. Furthermore, the column densities of CHD_2OH are about a factor 3–10 lower than that of CH_2DOH , see Fig. 4. In order to translate the column density ratios to the D/H ratios, statistical weighting has to be taken into account since a deuterium atom has a three times higher probability to land in the CH_3 group compared to the OH group. Therefore, the D/H ratios of CH_3OH and CH_2DOH can be derived through,

$$N_{\text{CH}_2\text{DOH}}/N_{\text{CH}_3\text{OH}} = 3(\text{D}/\text{H})_{\text{CH}_3\text{OH}}, \quad (2)$$

$$N_{\text{CHD}_2\text{OH}}/N_{\text{CH}_2\text{DOH}} = (\text{D}/\text{H})_{\text{CH}_2\text{DOH}}. \quad (3)$$

The derived D/H ratios are also listed in Table B.1.

The resulting $(\text{D}/\text{H})_{\text{CH}_3\text{OH}}$ and $(\text{D}/\text{H})_{\text{CH}_2\text{DOH}}$ ratios are presented in Figs. 3 and 4, respectively. Including upper limits, a (limit on the) $(\text{D}/\text{H})_{\text{CH}_3\text{OH}}$ and $(\text{D}/\text{H})_{\text{CH}_2\text{DOH}}$ ratios could be derived for 38 and 26 of the 99 studied sources, respectively. Besides the ALMAGAL sources, also other classical high-mass hot

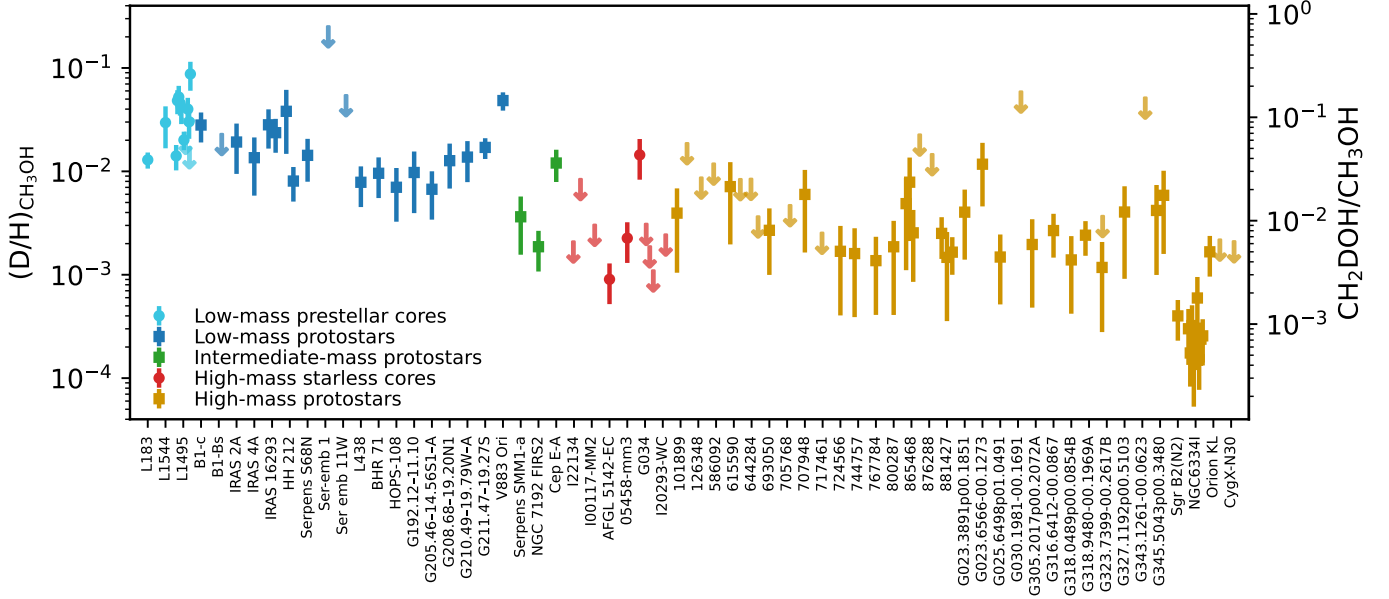


Fig. 3. The $(D/H)_{CH_3OH}$ ratio (squares) derived from the N_{CH_2DOH}/N_{CH_3OH} for low-mass, intermediate-mass, and high-mass protostellar systems including data from both this study and the literature (see Appendix C for references). Only D/H ratios derived from interferometric observations are included to minimize effects of beam dilution and to exclude any contribution from larger scales. Also data for low-mass prestellar cores and high-mass starless cores (circles) from the literature (including observations with single dish telescopes) are included. Upper limits are presented as arrows.

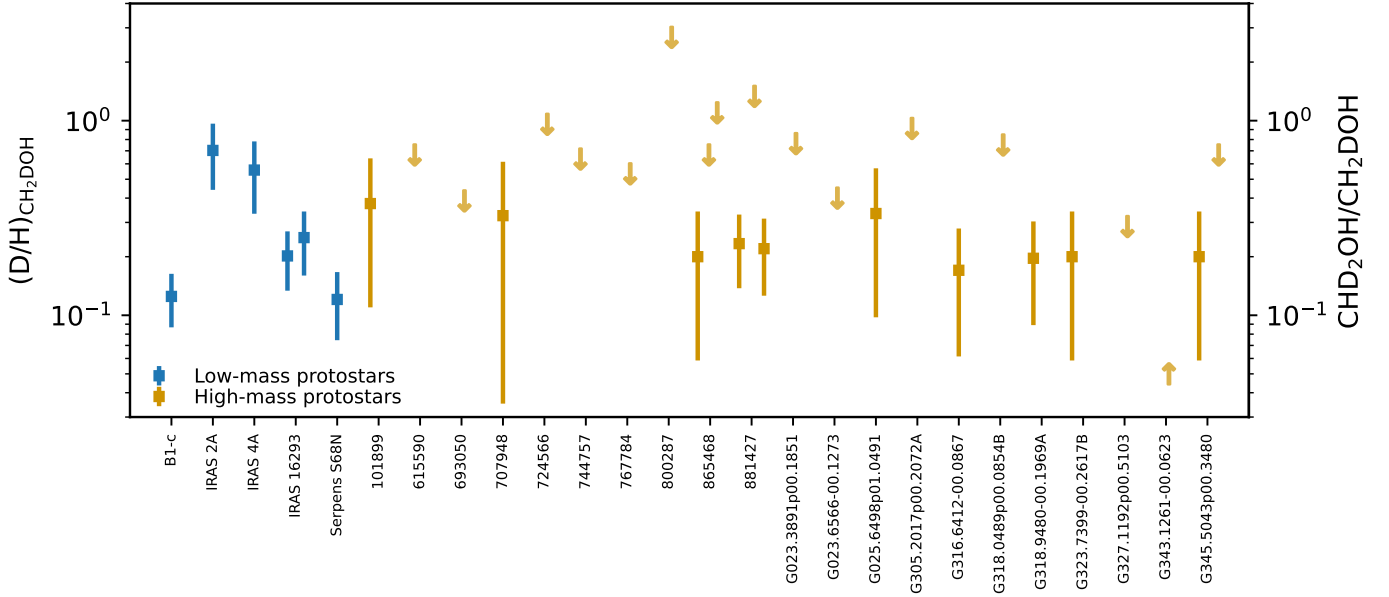


Fig. 4. The $(D/H)_{CH_2DOH}$ ratio derived from the N_{CHD_2OH}/N_{CH_2DOH} for low-mass and high-mass protostellar systems including data from both this study and the literature (see Appendix C for references). Upper and lower limits are presented as arrows. Only D/H ratios derived from interferometric observations are included to minimize effects of beam dilution and to exclude any contribution from larger scales. The $(D/H)_{CH_2DOH}$ of IRAS 2A and IRAS 4A were derived using older spectroscopic data (Taquet et al. 2019).

cores such as Sgr B2(N2) (Belloche et al. 2016), NGC 6334I (Bøgelund et al. 2018), Orion KL (Neill et al. 2013), and CygX-N30 (van der Walt et al. 2021) are included in Figs. 3 and 4. Only sources where N_{CH_3OH} is derived from the ^{13}C or ^{18}O isotopologues are included in Fig. 3 to ensure that N_{CH_3OH} is not underestimated. The $(D/H)_{CH_3OH}$ ratios lie mostly in the $10^{-2} - 10^{-4}$ range. Interestingly, all the ALMAGAL sources and Orion KL show higher $(D/H)_{CH_3OH}$ ratios ($10^{-2} - 10^{-3}$) than Sgr B2(N2) and NGC 6334I ($10^{-3} - 10^{-4}$). No clear correlation between

the detection of CH_2OH or the derived $(D/H)_{CH_3OH}$ and protostellar parameters such as L_{bol} and envelope mass is present among the high-mass sources. Excluding upper limits, the average $(D/H)_{CH_3OH}$ ratio is $1.1 \pm 0.7 \times 10^{-3}$. This is almost two orders of magnitude higher than the D/H ratio in the local ISM of $\sim 2 \times 10^{-5}$ (Linsky et al. 2006; Prodanović et al. 2010), suggesting effective deuteration in the cold high-mass prestellar phases. However, both the range of observed $(D/H)_{CH_3OH}$ values and the average is more than one order of magnitude lower than what is

generally observed toward low-mass sources ($\sim \text{few} \times 10^{-2}$, e.g., Bianchi et al. 2017a,b, 2020; Jacobsen et al. 2019; van Gelder et al. 2020, see Sect. 4.1 for further discussion).

Interestingly, the $(\text{D}/\text{H})_{\text{CH}_2\text{DOH}}$ ratio (Eq. (3)) is significantly higher than the $(\text{D}/\text{H})_{\text{CH}_3\text{OH}}$ ratio, see Fig. 4. For the high-mass sources, only ALMAGAL datapoints are shown since no other interferometric studies of CHD_2OH in high-mass protostellar systems are available. The derived $(\text{D}/\text{H})_{\text{CH}_2\text{DOH}}$ ratios lie mostly in the $0.1 - 1$ range, with an average of $2.0 \pm 0.8 \times 10^{-1}$, which is more than two orders of magnitude higher than the $(\text{D}/\text{H})_{\text{CH}_3\text{OH}}$ ratio. Furthermore, this indicates that about 1/5 of the single deuterated methanol molecules gets successively deuterated further toward CH_2DOH in high-mass protostellar systems. This is in good agreement with low-mass protostellar systems where about 1/4 of the CH_2DOH is successively deuterated toward CHD_2OH (Drozdovskaya et al. 2022).

4. Discussion

4.1. Methanol deuteration from low to high mass

In this work, a (limit on the) $(\text{D}/\text{H})_{\text{CH}_3\text{OH}}$ ratio could be derived for 38 of the 99 studied high-mass sources. Since large samples of both low-mass and high-mass protostellar systems with methanol D/H values are now available, a more significant comparison over the mass regime can be made. In Fig. 3, also $(\text{D}/\text{H})_{\text{CH}_3\text{OH}}$ ratios derived for both low-mass prestellar cores and high-mass starless cores are included. It is evident that the $(\text{D}/\text{H})_{\text{CH}_3\text{OH}}$ ratio is lower in high-mass hot cores ($10^{-4} - 10^{-2}$) than in their low-mass counterpart ($10^{-2} - 10^{-1}$). Intermediate-mass protostars show values in between ($10^{-3} - 10^{-2}$), but this subsample only consists of three sources (NGC 7192 FIR2, Cep E-A, and Serpens SMM1-a, Fuente et al. 2014; Ospina-Zamudio et al. 2018; Ligterink et al. 2022, the D/H ratio of NGC 7192 FIR2 is taken from the beam averaged values). However, interestingly the $(\text{D}/\text{H})_{\text{CH}_2\text{DOH}}$ ratio seems very similar between low-mass protostars and high-mass protostars ($0.1 - 1$, see Fig. 4). Among the low-mass sources, IRAS 2A and IRAS 4A show somewhat elevated $(\text{D}/\text{H})_{\text{CH}_2\text{DOH}}$, but these were derived using older spectroscopic data of CHD_2OH (Taquet et al. 2019).

In Fig. 5, the mean $(\text{D}/\text{H})_{\text{CH}_3\text{OH}}$ ratio is presented for low-mass, intermediate-mass, and high-mass protostellar systems. The average $(\text{D}/\text{H})_{\text{CH}_3\text{OH}}$ ratio for high-mass hot cores ($1.1 \pm 0.7 \times 10^{-3}$) lies more than one order of magnitude lower than the average ratio for low-mass hot corinos ($2.2 \pm 1.2 \times 10^{-2}$), with the average $(\text{D}/\text{H})_{\text{CH}_3\text{OH}}$ for intermediate-mass protostars in between ($8.9 \pm 7.4 \times 10^{-3}$). A similar trend is seen for the high-mass and low-mass prestellar phases where the average $(\text{D}/\text{H})_{\text{CH}_3\text{OH}}$ ratios are $5.9 \pm 5.1 \times 10^{-3}$ and $3.4 \pm 1.9 \times 10^{-2}$, respectively. The lower $(\text{D}/\text{H})_{\text{CH}_3\text{OH}}$ ratio in both high-mass hot cores and high-mass prestellar phases compared to their lower-mass counterparts suggests a lower deuteration efficiency already in the high-mass prestellar phases (see Sect. 4.3).

The methanol D/H ratios derived in low-mass prestellar cores agree well with those derived for low-mass protostars (see Fig. 3). Since CH_3OH is formed through the hydrogenation of CO ice (e.g., Watanabe & Kouchi 2002; Fuchs et al. 2009; Simons et al. 2020; Santos et al. 2022), this is a strong indication for inheritance of methanol and other COMs ices between low-mass prestellar phases and protostars. On the other hand, the average $(\text{D}/\text{H})_{\text{CH}_3\text{OH}}$ ratio for high-mass starless cores ($5.9 \pm 5.1 \times 10^{-3}$) seems to be about a factor of five higher than that for high-mass protostars ($1.1 \pm 0.7 \times 10^{-3}$). However, the average $(\text{D}/\text{H})_{\text{CH}_3\text{OH}}$ of the high-mass starless cores has a

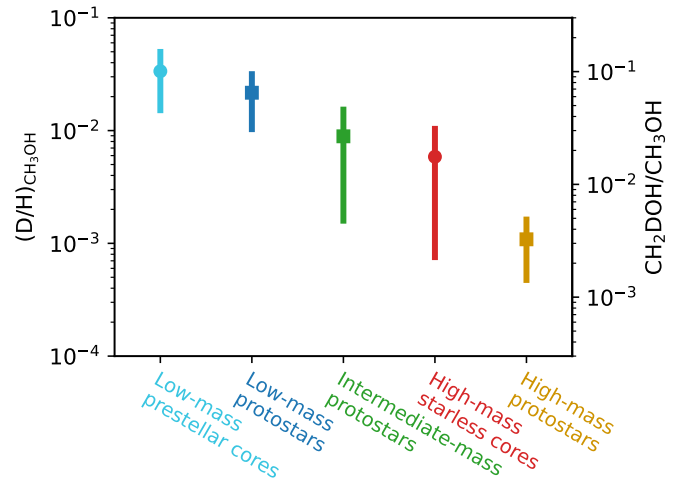


Fig. 5. The average $(\text{D}/\text{H})_{\text{CH}_3\text{OH}}$ ratio derived from $N_{\text{CH}_2\text{DOH}}/N_{\text{CH}_3\text{OH}}$ for low-mass, intermediate-mass, and high-mass protostellar systems and low-mass prestellar cores and high-mass starless cores. The prestellar phases are indicated with circles and the protostellar phases with squares.

large errorbar since it is based on three detections of which one (G034-G2(MM2)) has a high $(\text{D}/\text{H})_{\text{CH}_3\text{OH}}$ ratio of $\sim 10^{-2}$ (Fontani et al. 2015). The other two detections (AFGL 5142-EC and 0548-mm3; Fontani et al. 2015) and all the upper limits show $\text{D}/\text{H} \lesssim 2 \times 10^{-3}$ which agree well with most of the ALMAGAL sources as well as with Orion KL (Neill et al. 2013). Only Sgr B2(N2) and most of the cores in NGC 6334I show slightly lower D/H ratios at the 10^{-4} level. This therefore also suggests inheritance of methanol ice from the high-mass prestellar phase to the protostellar phase.

4.2. Singly vs doubly deuterated methanol

As evident from Figs. 3 and 4, the methanol D/H ratio derived for CH_2DOH is significantly higher than that derived for CH_3OH . The average $(\text{D}/\text{H})_{\text{CH}_2\text{DOH}}$ ratio is about two orders of magnitude higher ($2.0 \pm 0.8 \times 10^{-1}$) than $(\text{D}/\text{H})_{\text{CH}_3\text{OH}}$. In contrast to $(\text{D}/\text{H})_{\text{CH}_3\text{OH}}$, this is in good agreement with the average of $3.0 \pm 2.0 \times 10^{-1}$ for low-mass protostars, suggesting that successive deuteration happens almost equally effective in both low-mass and high-mass systems.

Having higher D/H ratios for the doubly deuterated isotopologue compared with singly deuterated isotopologue is not unique to methanol. For water, the $\text{D}_2\text{O}/\text{HDO}$ ratios are on the order of 10^{-2} (e.g., Coutens et al. 2014; Jensen et al. 2021), which is about an order of magnitude higher than typical $\text{HDO}/\text{H}_2\text{O}$ ratios ($\lesssim 10^{-3}$; Persson et al. 2014; Jensen et al. 2019; van't Hoff et al. 2022). This difference was attributed to be the result of layered ice chemistry (Dartois et al. 2003; Furuya et al. 2016), where the bulk of the water ice is formed in the warmer translucent cloud phase with a low D/H ratio whereas the surface layers formed in the cold prestellar phases show higher D/H ratios. However, methanol is thought to only start forming in the cold prestellar phases where CO is frozen out (e.g., Watanabe & Kouchi 2002; Fuchs et al. 2009) with little to no formation in the warmer translucent phases. Indeed, also for a direct precursor of CH_3OH on the surface of dust grains, H_2CO , the $\text{D}_2\text{CO}/\text{HDCO}$ ratio in IRAS 16293-2422 points toward a high D/H ratio of $\sim 25\%$ compared to a much lower D/H ratio de-

rived from HDCO/H₂CO ($\sim 3\%$; Persson et al. 2018). Small variations in temperature in the 10–20 K range can change the D/H ratio of ice mantle species such as methanol (see Sect. 4.3), but this should affect both CH₂DOH and CHD₂OH in a similar way and should therefore not lead to the observed difference.

One possible explanation could be the optical depth of CH₂DOH. In the low-mass source L1551 IRS5, the emission of CH₂DOH (as well as ¹³CH₃OH) was suggested to be optically thick (Bianchi et al. 2020). However, since the (D/H)_{CH₃OH} ratios derived from CH₂DOH clearly show lower values in high-mass protostellar systems compared to their lower-mass counterpart (see Sect. 4.1), this does not seem like a viable solution. Very recently, spectroscopic data for ¹³CH₂DOH has become available (Ohno et al. 2022), but these do not yet include a calculation of the partition function and line properties such as A_{ij} . When assuming that the source size is equal to the beam size, the line optical depth of the most constraining transition, ($17_{1,16} e_0 - 17_{0,17} e_0$, $E_{up} = 336$ K) is $\tau < 10^{-2}$. Only for source sizes smaller than $< 0.5''$ does CH₂DOH become marginally optically thick ($\tau > 0.1$) for the most line rich sources. Also, the (D/H)_{CH₃OH} ratios where N_{CH_3OH} was derived from the possibly optically thick ¹³C isotopologue are on average less than a factor ~ 3 higher than the (D/H)_{CH₃OH} ratios where N_{CH_3OH} could be derived using the optically thin ¹⁸O isotopologue (see Fig. E.1).

A more realistic explanation is that successive deuteration of molecules is more effective than the first deuteration. This explanation is supported by several laboratory studies performed at low temperatures of 10–20 K (e.g., Nagaoka et al. 2005, 2007; Hidaka et al. 2009). Drozdovskaya et al. (2022) showed that their observed (D/H)_{CH₃OH} ratio as derived from CH₂DOH for the low-mass binary IRAS 16293-2422 could be well explained by these experiments whereas CHD₂OH and CD₃OH were overproduced by the experiments. The latter could be the result of the high atomic D/H flux of 0.1 used in the laboratory studies in contrast to the ISM value of $\sim 10^{-5}$, although the atomic D/H ratio is enhanced in cold dense prestellar cores. Assuming that the (D/H)_{CH₃OH} ratio is a direct representative of the gaseous atomic D/H ratio available in the prestellar phases (i.e., that H/D addition reactions are equally effective), a D/H flux of $\sim 10^{-3}$ may be more realistic for high-mass cold dense cores.

4.3. Linking the methanol D/H to the physical conditions during formation

Given the sensitivity of the methanol deuteration process to both temperature and density (i.e., CO freeze-out), the measured methanol D/H ratios are linked to these physical properties during the prestellar phases. To quantify this for the protostellar systems studied in this work, the observed D/H ratios are compared to the astrochemical gas-grain models presented by Bøgelund et al. (2018) and Taquet et al. (2019). These works used the GRAINOBLE model (Taquet et al. 2012, 2013, 2014) to test the effect of the dust and gas temperature T (assumed to be equal) and hydrogen density $n_H = n(H) + 2n(H_2)$ on the resulting (D/H)_{CH₃OH} ratio in the ices during the prestellar phases. In this work, we compare our results to their results and therefore only a brief description of the model is presented.

In GRAINOBLE, the gas-ice chemistry is computed in three phases: the bulk ice, the ice surface layers, and in the gas phase, following the approach initially presented by Hasegawa & Herbst (1993). The model includes both adsorption and desorption reactions and computes the rate equations in each phase. The chemical network used for the gas-phase chemistry is described in Taquet et al. (2014) and includes both ion-neutral chemistry

and all molecules relevant for the chemistry of methanol (e.g., CO, HCO, H₂CO). Moreover, the model computes the deuteration of ice species based on laboratory experiments and includes both the hydrogenation (with both H and D atoms) reactions leading to methanol as well as hydrogen/deuterium abstraction reactions in low temperature ($\sim 10 - 15$ K) conditions (Hidaka et al. 2009).

The effect of T and n_H on the resulting methanol D/H ratio is presented in Fig. 6 as computed by Bøgelund et al. (2018) and Taquet et al. (2019). For a constant temperature and density, the chemistry is evolved over a timescale indicated on the top of each panel, where the free-fall timescale t_{FF} is 4.4×10^5 , 1.4×10^5 , and 4.4×10^4 years for $n_H = 10^4$, 10^5 , and 10^6 cm⁻³, respectively. For the longest timescales ($t = 10t_{FF}$), it is evident that for all densities the methanol D/H ratio drops with increasing temperature. The strongest decrease is seen for 10^6 cm⁻³, where the methanol D/H ratio decreases from $\sim 6 \times 10^{-2}$ for $T = 10$ K to as low as $\sim 10^{-4}$ when $T = 30$ K. A similar trend is visible for 10^5 cm⁻³ where the D/H ratio decreases from $\sim 2 \times 10^{-2}$ for $T = 10$ K to $\sim 4 \times 10^{-4}$ at $T \sim 30$ K. The decreasing D/H ratios for both these densities is the direct consequence of the decrease of atomic deuterium enhancement in Eq. (1) with increasing temperature. For $n_H = 10^4$ cm⁻³, the methanol D/H ratio also decreases with temperature, but only by a factor ~ 4 between 10–30 K.

Another interesting trend is that for decreasing timescales (i.e., moving from right to left in Fig. 6), the D/H ratio at a given temperature also drops for all densities. The strongest drops are seen for the higher density cases at low temperatures (< 15 K) where the D/H ratio drops two orders of magnitude from $t = 10t_{FF}$ toward $t = 0.1t_{FF}$. This is the direct result of having less time where CO is frozen out and hence less time to deuterate ice species such as methanol. For higher temperatures ($T > 20$ K), this effect is less evident since significantly less CO freezes out, although a slightly higher binding energy of CO (up to ~ 1300 K; Noble et al. 2012) could result in CO frozen out till higher temperatures of ~ 25 K and hence a higher deuteration efficiency also above 20 K. However, even when CO does not freeze out, CO molecules can still land on the grain for a short period and react with H or D atoms toward HCO, H₂CO, and eventually (deuterated) methanol. This effect is most efficient for higher densities of $10^5 - 10^6$ cm⁻³ and reduces when timescales smaller than the free-fall timescale are considered. For the lowest density of 10^4 cm⁻³, this effect is most evident since the CO freeze-out timescale is the highest and therefore the methanol deuteration is hampered the most.

Overplotted in Fig. 6 are the observed methanol (D/H)_{CH₃OH} ratios for both low-mass and high-mass protostars. It is evident that the observed (D/H)_{CH₃OH} ratios suggest a different temperature during methanol formation or different prestellar phase lifetimes for low-mass and high-mass protostars. For high-mass protostars, a temperature of > 20 K is needed when the density is larger than 10^5 cm⁻³ and the timescale of the high-mass prestellar phase is $> t_{FF}$. A lower temperature of > 13 K at low densities of 10^4 cm⁻³ can also explain the observed methanol D/H ratio toward high-mass protostars, but such low densities in the dense high-mass starless phase are unlikely. Alternatively, the temperature in the high-mass prestellar phases can be in the $15 < T < 20$ K range with a lifetime of $\lesssim t_{FF}$. For prestellar lifetimes much smaller than the free-fall timescale, any temperature can explain the observed methanol deuteration toward high-mass protostars.

Contrary to the high-mass protostars, the observed (D/H)_{CH₃OH} ratio for low-mass protostars suggests both a temperature of < 15 K and a prestellar phase duration longer

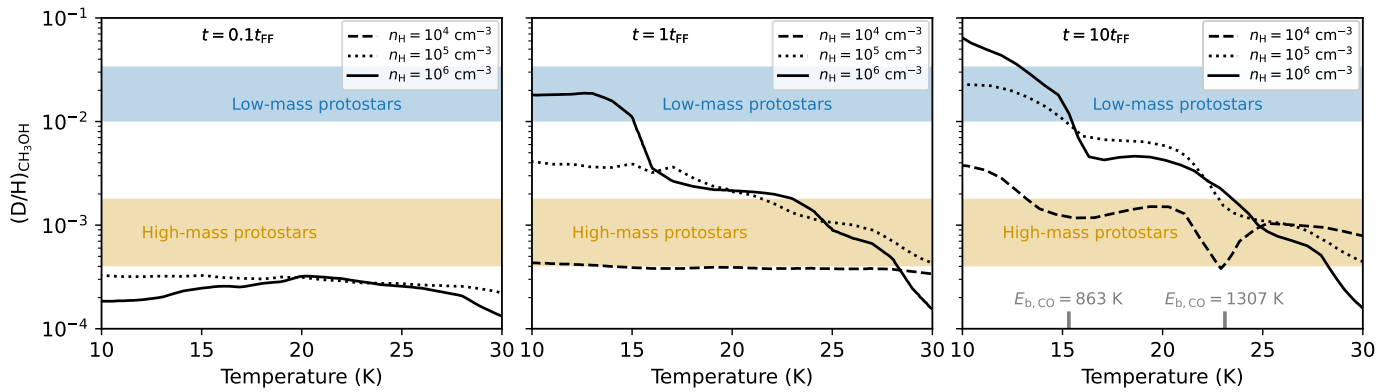


Fig. 6. The $(D/H)_{CH_3OH}$ ratio in the ices as function of the gas and dust temperature for $n_H = 10^4$ (dashed), 10^5 (dotted), and 10^6 cm^{-3} (solid) as modeled by [Bøgelund et al. \(2018\)](#) and [Taquet et al. \(2019\)](#) using the GRAINOBLE model ([Taquet et al. 2012, 2013, 2014](#)). The model results are shown for 0.1 (left), 1 (middle), and 10 (right) times free-fall timescales t_{FF} . The observed average $(D/H)_{CH_3OH}$ ratios are indicated in blue and orange for the low-mass and high-mass protostars, respectively. In the right panel, the range of possible desorption temperature of CO ice is indicated with the gray bars for binding energies between 863 K and 1307 K for CO ice deposited on non-porous amorphous solid water ([Noble et al. 2012](#)).

than $\geq t_{FF}$. Furthermore, the observed methanol D/H ratio for low-mass protostars can not be explained by a low density of 10^4 cm^{-3} at any modeled timescale.

It is important to note that the methanol D/H ratio is observed in the gas phase with ALMA whereas the GRAINOBLE models predict the ice abundances in the prestellar phases. Several processes can affect the D/H ratio as the ices warm up while infalling toward the protostar (e.g., [Ratajczak et al. 2009](#); [Faure et al. 2015](#)). However, one of the likely dominant processes, CH_2DOH formation through H-D substitution in methanol ice ([Nagaoka et al. 2005](#)) is included in the model but this does not dominate over hydrogenation of CO.

These results thus suggest that the high-mass prestellar phases are generally either warm ($T \gtrsim 20$ K) or short ($t \lesssim t_{FF}$) while the low-mass prestellar phases are colder ($T < 15$ K) and long ($t \gtrsim t_{FF}$). The observed methanol D/H ratios toward high-mass starless cores and low-mass prestellar cores also fit this picture, see Fig. E.2. On the other hand, the spread in observed abundance ratios of nitrogen-bearing COMs suggests that the scatter in timescales of high-mass prestellar phases is rather small and similar to that of low-mass prestellar phases ([Nazari et al. 2022](#)), implying that warmer high-mass pre-stellar phases are a more likely explanation. One possible explanation for the discrepancy between the low-mass and high-mass methanol D/H ratios could be that high-mass stars generally form in clusters with other nearby high-mass stars that heat the surrounding cloud which can affect the D/H ratios molecules forming in the ices (e.g., such as seen for water toward low-mass protostars; [Jensen et al. 2019](#)). The majority of the sources studied in this work are located in a clustered environments but these do not show significantly lower D/H ratios than high-mass sources that are single sources at our angular resolution. More modeling work similar to those performed by [Bøgelund et al. \(2018\)](#) and [Taquet et al. \(2019\)](#) including CHD_2OH is needed to further test these hypotheses.

5. Conclusion

In this work, (limits on) the D/H ratios of CH_3OH and CH_2DOH are determined for 38 and 26 sources, respectively, out of the 99 studied sources using ALMA observations of CH_2DOH , CHD_2OH , CH_3OH , $^{13}CH_3OH$, and $CH_3^{18}OH$. The de-

rived $(D/H)_{CH_3OH}$ and $(D/H)_{CH_2DOH}$ ratios are compared to each other as well as to other high-mass protostars, low-mass protostars, and both low-mass and high-mass prestellar phases. Furthermore, comparison with the gas-grain chemical code GRAINOBLE links the observed D/H ratios to the temperature during methanol formation and the lifetime of the prestellar phases. The main conclusions of this work are as follows:

- The $(D/H)_{CH_3OH}$ ratios of the high-mass protostars studied in this work lie in the $10^{-3} - 10^{-2}$ range. Combining our sample with other high-mass protostars studied with ALMA, an average $(D/H)_{CH_3OH}$ ratio of $1.1 \pm 0.7 \times 10^{-3}$ is derived. This is in good agreement with the $(D/H)_{CH_3OH}$ ratio derived for high-mass starless cores ($5.9 \pm 5.1 \times 10^{-3}$), but is more than an order of magnitude lower than the average $(D/H)_{CH_3OH}$ ratio for low-mass protostars ($2.2 \pm 1.2 \times 10^{-2}$) and low-mass prestellar cores ($3.4 \pm 1.9 \times 10^{-2}$).
- For $(D/H)_{CH_2DOH}$, significantly higher values than $(D/H)_{CH_3OH}$ are found ranging from 0.1–1 with an average of $2.0 \pm 0.8 \times 10^{-1}$. The latter is in good agreement with results on low-mass protostars and suggests that about 1/5 singly deuterated methanol molecules gets successively deuterated further independent of the mass of the system.
- Based on a comparison with GRAINOBLE models in the literature, the lower $(D/H)_{CH_3OH}$ ratios toward high-mass protostars suggest either a temperature of $\gtrsim 20$ K in the high-mass prestellar phases or a short lifetime ($\lesssim t_{FF}$) of the high-mass prestellar phases. This is in strong contrast with the low-mass sources for which the higher $(D/H)_{CH_3OH}$ ratio can only be achieved when the low-mass prestellar phases are both cold (< 15 K) and long lived ($\gtrsim t_{FF}$).

This work demonstrates that the deuteration of the CH_3 -group of methanol as measured toward protostellar systems could be used to probe the physical conditions (e.g., temperature) of the prestellar phases. The discrepancy in $(D/H)_{CH_3OH}$ between low-mass and high-mass sources indicates that the physical conditions are already different before the onset of star formation. Additional observations of multiple deuterated methanol isotopologues (e.g., CHD_2OH , CD_3OH) as well as CH_3OD will shed further light on the efficiency of methanol deuteration between low-mass and high-mass systems. In combination with additional modeling studies (such as those performed by [Bøgelund](#)

et al. 2018; Taquet et al. 2019; Kulterer et al. 2022), this can provide further insight on the relevant deuterium chemistry and how the D/H ratio varies across the protostellar mass range.

Acknowledgements. The authors would like to thank the anonymous referee for their constructive comments on the manuscript and L. Coudert for discussions on the CH₂DOH spectroscopy. This paper makes use of the following ALMA data: ADS/JAO.ALMA#2017.1.01174.S, ADS/JAO.ALMA#2019.1.00195.L. ALMA is a partnership of ESO (representing its member states), NSF (USA) and NINS (Japan), together with NRC (Canada), MOST and ASIAA (Taiwan), and KASI (Republic of Korea), in cooperation with the Republic of Chile. The Joint ALMA Observatory is operated by ESO, AUI/NRAO and NAOJ. Astrochemistry in Leiden is supported by the Netherlands Research School for Astronomy (NOVA), by funding from the European Research Council (ERC) under the European Union's Horizon 2020 research and innovation programme (grant agreement No. 101019751 MOLDISK), and by the Dutch Research Council (NWO) grants TOP-1 614.001.751, 648.000.022, and 618.000.001. Support by the Danish National Research Foundation through the Center of Excellence "InterCat" (Grant agreement no.: DNRF150) is also acknowledged.

References

- Aikawa, Y. & Herbst, E. 1999, *ApJ*, 526, 314
- Ambrose, H. E., Shirley, Y. L., & Scibelli, S. 2021, *MNRAS*, 501, 347
- Belloche, A., Müller, H. S. P., Garrod, R. T., & Menten, K. M. 2016, *A&A*, 587, A91
- Bianchi, E., Chandler, C. J., Ceccarelli, C., et al. 2020, *MNRAS*, 498, L87
- Bianchi, E., Codella, C., Ceccarelli, C., et al. 2017a, *MNRAS*, 467, 3011
- Bianchi, E., Codella, C., Ceccarelli, C., et al. 2017b, *A&A*, 606, L7
- Bizzocchi, L., Caselli, P., Spezzano, S., & Leonardo, E. 2014, *A&A*, 569, A27
- Bøgelund, E. G., Barr, A. G., Taquet, V., et al. 2019, *A&A*, 628, A2
- Bøgelund, E. G., McGuire, B. A., Ligterink, N. F. W., et al. 2018, *A&A*, 615, A88
- Brown, P. D. & Millar, T. J. 1989, *MNRAS*, 237, 661
- Caselli, P. & Ceccarelli, C. 2012, *A&A Rev.*, 20, 56
- Ceccarelli, C., Caselli, P., Bockelée-Morvan, D., et al. 2014, in *Protostars and Planets VI*, ed. H. Beuther, R. S. Klessen, C. P. Dullemond, & T. Henning, 859
- Chahine, L., López-Sepulcre, A., Neri, R., et al. 2022, *A&A*, 657, A78
- Coudert, L. H., Motiyenko, R. A., Margulès, L., & Tchana Kwabia, F. 2021, *Journal of Molecular Spectroscopy*, 381, 111515
- Coudert, L. H., Zemouli, M., Motiyenko, R. A., Margulès, L., & Klee, S. 2014, *J. Chem. Phys.*, 140, 064307
- Coutens, A., Jørgensen, J. K., Persson, M. V., et al. 2014, *ApJ*, 792, L5
- Dartois, E., Thi, W. F., Geballe, T. R., et al. 2003, *A&A*, 399, 1009
- Drozdovskaya, M. N., Coudert, L. H., Margulès, L., et al. 2022, *A&A*, 659, A69
- Drozdovskaya, M. N., Schroeder, I. R. H. G., Rubin, M., et al. 2021, *MNRAS*, 500, 4901
- Elia, D., Merello, M., Molinari, S., et al. 2021, *MNRAS*, 504, 2742
- Elia, D., Molinari, S., Schisano, E., et al. 2017, *MNRAS*, 471, 100
- Endres, C. P., Schlemmer, S., Schilke, P., Stutzki, J., & Müller, H. S. P. 2016, *Journal of Molecular Spectroscopy*, 327, 95
- Faure, A., Faure, M., Theulé, P., Quirico, E., & Schmitt, B. 2015, *A&A*, 584, A98
- Fisher, J., Paciga, G., Xu, L.-H., et al. 2007, *Journal of Molecular Spectroscopy*, 245, 7
- Fontani, F., Busquet, G., Palau, A., et al. 2015, *A&A*, 575, A87
- Fuchs, G. W., Cuppen, H. M., Ioppolo, S., et al. 2009, *A&A*, 505, 629
- Fuente, A., Cernicharo, J., Caselli, P., et al. 2014, *A&A*, 568, A65
- Furuya, K., van Dishoeck, E. F., & Aikawa, Y. 2016, *A&A*, 586, A127
- Hasegawa, T. I. & Herbst, E. 1993, *MNRAS*, 263, 589
- Hidaka, H., Watanabe, M., Kouchi, A., & Watanabe, N. 2009, *ApJ*, 702, 291
- Hsu, S.-Y., Liu, S.-Y., Liu, T., et al. 2022, *ApJ*, 927, 218
- Ilyushin, V. V., Müller, H. S. P., Jørgensen, J. K., et al. 2022, *A&A*, 658, A127
- Jacobsen, S. K., Jørgensen, J. K., Di Francesco, J., et al. 2019, *A&A*, 629, A29
- Jensen, S. S., Jørgensen, J. K., Kristensen, L. E., et al. 2021, *A&A*, 650, A172
- Jensen, S. S., Jørgensen, J. K., Kristensen, L. E., et al. 2019, *A&A*, 631, A25
- Jørgensen, J. K., Müller, H. S. P., Calcutt, H., et al. 2018, *A&A*, 620, A170
- Kulterer, B. M., Drozdovskaya, M. N., Antonellini, S., Walsh, C., & Millar, T. J. 2022, *ACS Earth and Space Chemistry*, 6, 1171
- Lattanzi, V., Bizzocchi, L., Vasyunin, A. I., et al. 2020, *A&A*, 633, A118
- Lee, C.-F., Codella, C., Li, Z.-Y., & Liu, S.-Y. 2019a, *ApJ*, 876, 63
- Lee, J.-E., Lee, S., Baek, G., et al. 2019b, *Nature Astronomy*, 3, 314
- Ligterink, N. F. W., Ahmadi, A., Coutens, A., et al. 2021, *A&A*, 647, A87
- Ligterink, N. F. W., Ahmadi, A., Luitel, B., et al. 2022, *ACS Earth and Space Chemistry*, 6, 455
- Linsky, J. L., Draine, B. T., Moos, H. W., et al. 2006, *ApJ*, 647, 1106
- Manigand, S., Jørgensen, J. K., Calcutt, H., et al. 2020, *A&A*, 635, A48
- Martín-Doménech, R., Bergner, J. B., Öberg, K. I., et al. 2021, *ApJ*, 923, 155
- Martín-Doménech, R., Bergner, J. B., Öberg, K. I., & Jørgensen, J. K. 2019, *ApJ*, 880, 130
- McMullin, J. P., Waters, B., Schiebel, D., Young, W., & Golap, K. 2007, in *Astronomical Society of the Pacific Conference Series*, Vol. 376, *Astronomical Data Analysis Software and Systems XVI*, ed. R. A. Shaw, F. Hill, & D. J. Bell, 127
- Mège, P., Russeil, D., Zavagno, A., et al. 2021, *A&A*, 646, A74
- Milam, S. N., Savage, C., Brewster, M. A., Ziurys, L. M., & Wyckoff, S. 2005, *ApJ*, 634, 1126
- Molinari, S., Swinyard, B., Bally, J., et al. 2010, *A&A*, 518, L100
- Müller, H. S. P., Belloche, A., Xu, L.-H., et al. 2016, *A&A*, 587, A92
- Müller, H. S. P., Schlöder, F., Stutzki, J., & Winnewisser, G. 2005, *Journal of Molecular Structure*, 742, 215
- Müller, H. S. P., Thorwirth, S., Roth, D. A., & Winnewisser, G. 2001, *A&A*, 370, L49
- Nagaoka, A., Watanabe, N., & Kouchi, A. 2005, *ApJ*, 624, L29
- Nagaoka, A., Watanabe, N., & Kouchi, A. 2007, *Journal of Physical Chemistry A*, 111, 3016
- Nazari, P., Meijerhof, J., van Gelder, M., & van Dishoeck, E. F. 2022, *A&A*, submitted
- Nazari, P., van Gelder, M. L., van Dishoeck, E. F., et al. 2021, *A&A*, 650, A150
- Neill, J. L., Crockett, N. R., Bergin, E. A., Pearson, J. C., & Xu, L.-H. 2013, *ApJ*, 777, 85
- Noble, J. A., Congiu, E., Dulieu, F., & Fraser, H. J. 2012, *MNRAS*, 421, 768
- Ohno, Y., Oyama, T., Tamanai, A., et al. 2022, *ApJ*, 932, 101
- Ospina-Zamudio, J., Lefloch, B., Ceccarelli, C., et al. 2018, *A&A*, 618, A145
- Parise, B., Castets, A., Herbst, E., et al. 2004, *A&A*, 416, 159
- Parise, B., Ceccarelli, C., Tielens, A. G. G. M., et al. 2002, *A&A*, 393, L49
- Pearson, J. C., Yu, S., & Drouin, B. J. 2012, *Journal of Molecular Spectroscopy*, 280, 119
- Perotti, G., Jørgensen, J. K., Fraser, H. J., et al. 2021, *A&A*, 650, A168
- Perotti, G., Rocha, W. R. M., Jørgensen, J. K., et al. 2020, *A&A*, 643, A48
- Persson, M. V., Jørgensen, J. K., Müller, H. S. P., et al. 2018, *A&A*, 610, A54
- Persson, M. V., Jørgensen, J. K., van Dishoeck, E. F., & Harsono, D. 2014, *A&A*, 563, A74
- Pickett, H. M., Poynter, R. L., Cohen, E. A., et al. 1998, *J. Quant. Spectr. Rad. Transf.*, 60, 883
- Prodanović, T., Steigman, G., & Fields, B. D. 2010, *MNRAS*, 406, 1108
- Ratajczak, A., Quirico, E., Faure, A., Schmitt, B., & Ceccarelli, C. 2009, *A&A*, 496, L21
- Roberts, H., Herbst, E., & Millar, T. J. 2003, *ApJ*, 591, L41
- Santos, J. C., Chuang, K.-J., Lamberts, T., et al. 2022, *ApJ*, 931, L33
- Simons, M. A. J., Lamberts, T., & Cuppen, H. M. 2020, *A&A*, 634, A52
- Taquet, V., Bianchi, E., Codella, C., et al. 2019, *A&A*, 632, A19
- Taquet, V., Ceccarelli, C., & Kahane, C. 2012, *A&A*, 538, A42
- Taquet, V., Charnley, S. B., & Sipilä, O. 2014, *ApJ*, 791, 1
- Taquet, V., Peters, P. S., Kahane, C., et al. 2013, *A&A*, 550, A127
- Tielens, A. G. G. M. 1983, *A&A*, 119, 177
- Tielens, A. G. G. M. 2013, *Reviews of Modern Physics*, 85, 1021
- van der Walt, S. J., Kristensen, L. E., Jørgensen, J. K., et al. 2021, *A&A*, 655, A86
- van Dishoeck, E. F., Blake, G. A., Jansen, D. J., & Groesbeck, T. D. 1995, *ApJ*, 447, 760
- van Gelder, M. L., Nazari, P., Tabone, B., et al. 2022, *A&A*, 662, A67
- van Gelder, M. L., Tabone, B., Tychoniec, L., et al. 2020, *A&A*, 639, A87
- van't Hoff, M. L. R., Harsono, D., van Gelder, M. L., et al. 2022, *ApJ*, 924, 5
- Vastel, C., Bottinelli, S., Caux, E., Glorian, J. M., & Boiziot, M. 2015, in *SF2A-2015: Proceedings of the Annual meeting of the French Society of Astronomy and Astrophysics*, 313–316
- Watanabe, N. & Kouchi, A. 2002, *ApJ*, 571, L173
- Watson, W. D. 1974, *ApJ*, 188, 35
- Wilson, T. L. & Rood, R. 1994, *ARA&A*, 32, 191
- Xu, L.-H., Fisher, J., Lees, R. M., et al. 2008, *Journal of Molecular Spectroscopy*, 251, 305
- Xu, L.-H. & Lovas, F. J. 1997, *Journal of Physical and Chemical Reference Data*, 26, 17
- Yang, Y.-L., Evans, Neal J. I., Smith, A., et al. 2020, *ApJ*, 891, 61

Appendix A: Transitions of CH₃OH and isotopologues

Table A.1. Transitions of CH₃OH and isotopologues with $A_{ij} > 10^{-6}$ and $E_{up} < 1000$ K covered in the ALMAGAL (2019.1.00195.L) program.

Species	Transition		Frequency	A_{ij}	E_{up}
	(J K L M)	- (J K L M)	(GHz)	(s ⁻¹)	(K)
CH ₃ OH	6 1 5 3	- 7 2 5 3	217.2992	4.3×10^{-5}	373.9
	15 6 9 3	- 16 5 11 3	217.6427	1.9×10^{-5}	745.6
	15 6 10 3	- 16 5 12 3	217.6427	1.9×10^{-5}	745.6
	20 1 19 1	- 20 0 20 1	217.8865	3.4×10^{-5}	508.4
	4 2 3 1	- 3 1 2 1	218.4401	4.7×10^{-5}	45.5
	25 3 23 1	- 24 4 20 1	219.9837	2.0×10^{-5}	802.2
	23 5 18 1	- 22 6 17 1	219.9937	1.7×10^{-5}	775.9
	8 0 8 1	- 7 1 6 1	220.0786	2.5×10^{-5}	96.6
	10 5 6 2	- 11 4 8 2	220.4013	1.1×10^{-5}	251.6
¹³ CH ₃ OH	14 1 13 -0	- 13 2 12 -0	217.0446	2.4×10^{-5}	254.3
	10 2 8 +0	- 9 3 7 +0	217.3995	1.5×10^{-5}	162.4
	17 7 11 +0	- 18 6 12 +0	220.3218	1.3×10^{-5}	592.3
	17 7 10 -0	- 18 6 13 -0	220.3218	1.3×10^{-5}	592.3
CH ₃ ¹⁸ OH	14 1 14 1	- 13 2 12 1	217.1729	1.7×10^{-5}	238.9
	18 6 13 4	- 17 7 11 4	217.9223	1.5×10^{-5}	874.1
	17 5 13 4	- 18 6 13 4	218.5521	3.2×10^{-5}	884.6
	4 2 2 2	- 3 1 2 2	219.4078	4.6×10^{-5}	44.6
	8 7 1 5	- 7 6 1 5	219.8433	2.8×10^{-5}	663.2
	18 3 16 5	- 19 4 16 5	219.9572	5.1×10^{-5}	795.8
	8 1 8 1	- 7 0 7 1	220.1951	3.6×10^{-5}	85.7
CH ₂ DOH	26 4 22 0	- 26 3 24 2	217.2664	2.0×10^{-5}	817.1
	26 1 25 2	- 26 1 26 2	217.3300	1.1×10^{-5}	777.9
	17 4 13 2	- 16 5 11 1	217.3436	5.2×10^{-6}	409.7
	17 4 14 2	- 16 5 12 1	217.3593	5.3×10^{-6}	409.7
	23 6 18 1	- 22 7 15 0	217.3818	6.4×10^{-6}	742.6
	23 6 17 1	- 22 7 16 0	217.3825	6.4×10^{-6}	742.6
	18 1 17 2	- 18 2 17 0	217.4479	1.8×10^{-5}	391.5
	25 1 25 2	- 25 0 25 1	217.6429	4.7×10^{-5}	712.4
	12 7 6 0	- 13 6 7 1	217.6446	2.5×10^{-6}	357.2
	12 7 5 0	- 13 6 8 1	217.6446	2.5×10^{-6}	357.2
	18 0 18 0	- 17 1 16 2	218.1095	8.9×10^{-6}	363.2
	5 2 4 1	- 5 1 5 1	218.3164	9.1×10^{-6}	58.7
	24 3 21 1	- 24 2 23 2	218.5348	3.9×10^{-5}	687.7
	20 5 16 1	- 19 6 13 0	219.2043	1.5×10^{-5}	557.6
	20 5 15 1	- 19 6 14 0	219.2061	1.5×10^{-5}	557.6
	5 1 5 1	- 4 1 4 1	219.5515	7.0×10^{-6}	48.2
	5 1 5 0	- 4 1 4 0	220.0718	3.3×10^{-5}	35.8
	29 4 26 0	- 29 3 26 2	220.3492	2.5×10^{-5}	997.1
	17 1 16 0	- 17 0 17 0	220.5526	3.8×10^{-5}	335.9
	21 1 20 1	- 21 1 21 1	220.6256	2.0×10^{-6}	515.1
	21 2 19 2	- 21 1 20 2	220.7358	3.9×10^{-5}	531.1
CHD ₂ OH	6 2 2 1	- 5 1 2 2	217.0702	1.8×10^{-6}	61.9
	13 2 1 2	- 12 3 1 2	217.1181	8.8×10^{-6}	213.0
	16 5 1 2	- 17 4 1 0	217.2651	2.4×10^{-6}	366.8
	7 0 1 2	- 6 1 1 2	217.4912	2.9×10^{-5}	74.3
	7 4 2 1	- 8 3 2 0	217.4946	4.4×10^{-6}	111.1
	7 4 1 1	- 8 3 1 0	217.5430	4.4×10^{-6}	111.1
	24 9 1 1	- 25 8 1 0	217.8034	9.0×10^{-6}	854.9
	24 9 2 1	- 25 8 2 0	217.8034	9.0×10^{-6}	854.9
	2 2 1 1	- 3 1 1 0	218.0092	5.5×10^{-6}	25.8
	7 2 1 0	- 7 1 2 0	218.1279	1.2×10^{-5}	68.8
	16 3 2 2	- 15 4 2 2	218.2323	6.9×10^{-6}	318.2
	20 2 2 2	- 20 2 1 1	218.4156	9.0×10^{-6}	449.9

Table A.1. continued.

Species	Transition		Frequency (GHz)	A_{ij} (s^{-1})	E_{up} (K)
	(J K L M)	- (J K L M)			
	11 2 1 2	- 11 1 2 2	218.4824	2.3×10^{-5}	163.0
	12 2 1 2	- 12 1 2 2	219.2181	4.9×10^{-6}	187.0
	23 10 2 2	- 24 9 2 2	219.3323	5.1×10^{-6}	872.6
	23 10 1 2	- 24 9 1 2	219.3323	5.1×10^{-6}	872.6
	16 3 1 0	- 15 4 1 0	219.3377	6.5×10^{-6}	300.9
	22 5 2 0	- 22 4 1 2	219.6514	2.6×10^{-6}	583.5
	22 5 1 0	- 22 4 2 2	219.7983	2.5×10^{-6}	583.4
	13 2 1 0	- 12 3 1 0	220.2430	4.7×10^{-6}	195.3
	11 6 1 1	- 12 5 1 1	220.5567	1.1×10^{-6}	249.5
	11 6 2 1	- 12 5 2 1	220.5569	1.1×10^{-6}	249.5

Notes. The typical beam size is $\theta_{beam} \sim 1''$ and the typical rms is $rms_{line} \sim 0.2$ K.

Appendix B: Observational details

Table B.1. Column densities of $^{13}\text{CH}_3\text{OH}$, $\text{CH}_3^{18}\text{OH}$, CH_3OH , CH_2DOH , and CHD_2OH and derived methanol D/H ratios.

Source	RA (J2000)	Dec (J2000)	θ_{beam} ''	T_{ex} K	$N_{^{13}\text{CH}_3\text{OH}}$ cm^{-2}	$N_{\text{CH}_3^{18}\text{OH}}$ cm^{-2}	$N_{\text{CH}_3\text{OH}}$ cm^{-2}	$N_{\text{CH}_2\text{DOH}}$ cm^{-2}	$N_{\text{CHD}_2\text{OH}}$ cm^{-2}	(D/H) $_{\text{CH}_3\text{OH}}$ ¹	(D/H) $_{\text{CH}_2\text{DOH}}$ ²
86213A	18:26:48.92	-12:26:24.51	1.23	150	<3.3(15)	<1.0(15)	0.4–14.8(16)	<2.1(15)	<2.4(15)	–	–
86213B	18:26:47.96	-12:26:20.73	1.23	150	<4.0(15)	<1.6(15)	0.3–17.9(16)	<1.5(15)	<4.0(15)	–	–
86213C	18:26:48.73	-12:26:25.98	1.23	150	<1.9(15)	<1.1(15)	0.5–8.7(16)	<1.7(15)	<3.0(15)	–	–
81635A	18:25:00.82	-13:15:34.46	1.22	150	<3.8(15)	<2.8(15)	0.1–17.7(16)	<2.5(15)	<4.7(15)	–	–
81635B	18:25:01.01	-13:15:38.57	1.22	150	<2.7(15)	<1.5(15)	<1.4(15)	<3.1(15)	<2.2(15)	–	–
81635C	18:25:01.65	-13:15:28.99	1.22	150	<10.0(15)	<1.5(15)	<4.0(15)	<3.6(15)	<4.0(15)	–	–
83968A	18:25:10.59	-12:42:22.16	1.23	150	<2.2(15)	<1.4(15)	0.1–10.9(16)	<1.5(15)	<5.2(15)	–	–
83968B	18:25:10.69	-12:42:26.14	1.23	150	<3.0(15)	<1.2(15)	<1.5(15)	<1.7(15)	<5.1(15)	–	–
83968C	18:25:10.82	-12:42:24.68	1.23	150	<2.3(15)	<0.9(14)	0.1–11.3(16)	<1.9(15)	<3.2(15)	–	–
83968D	18:25:10.62	-12:42:19.43	1.23	150	<2.3(15)	<1.2(15)	<1.3(15)	<3.0(15)	<5.2(15)	–	–
83968E	18:25:10.65	-12:42:24.74	1.23	150	<2.3(15)	<1.2(15)	<1.3(15)	<2.4(15)	<5.0(15)	–	–
101899 C1	18:34:40.29	-09:00:38.44	1.25	150	1.5±0.3(16)	<4.0(15)	6.8±3.6(17)	8.0±4.0(15)	3.0±1.5(15)	3.9±2.9(-3)	3.8±2.7(-1)
101899 C2	18:34:40.29	-09:00:38.44	1.25	150	6.7±1.5(15)	<4.0(15)	2.9±1.6(17)	<6.0(15)	<3.0(15)	<1.5(-2)	–
103421	18:33:23.98	-08:33:31.92	1.24	150	<4.3(15)	<1.0(15)	0.1–1.9(17)	<3.3(15)	<2.4(15)	–	–
106756A	18:34:23.98	-07:54:48.26	1.23	150	<2.5(15)	<2.7(15)	0.2–11.2(16)	<3.5(15)	<3.8(15)	–	–
106756B	18:34:25.55	-07:54:46.39	1.23	150	<4.0(15)	<2.0(15)	<4.2(15)	<3.5(15)	<6.6(15)	–	–
106756C	18:34:25.59	-07:54:43.11	1.23	150	<1.1(16)	<2.6(15)	<4.3(15)	<3.5(15)	<8.0(15)	–	–
126120A	18:42:37.55	-04:02:05.17	1.17	150	<1.9(15)	<5.7(14)	0.5–9.1(16)	<1.7(15)	<2.4(15)	–	–
126120B	18:42:37.66	-04:02:07.27	1.17	150	<2.0(15)	<7.8(14)	0.3–9.5(16)	<1.8(15)	<4.1(15)	–	–
126120C	18:42:36.85	-04:02:17.66	1.17	150	<3.8(15)	<1.8(15)	<5.7(15)	<4.2(15)	<6.3(15)	–	–
126120D	18:42:37.14	-04:02:02.37	1.17	150	<3.4(15)	<0.9(14)	<1.0(15)	<2.0(15)	<2.9(15)	–	–
126348	18:42:51.98	-03:59:54.37	1.16	150	1.1±0.3(16)	3.0±2.0(15)	9.4±6.9(17)	<5.0(15)	<1.7(15)	<6.9(-3)	–
565926A	08:02:42.97	-34:31:48.77	0.58	150	<5.1(15)	<2.5(15)	<2.5(15)	<4.1(15)	<6.4(15)	–	–
565926B	08:02:42.94	-34:31:49.96	0.58	150	<5.0(15)	<2.4(15)	<4.5(15)	<6.2(15)	<4.9(15)	–	–
565926C	08:02:42.72	-34:31:49.61	0.58	150	<5.1(15)	<2.5(15)	<2.5(15)	<4.1(15)	<4.5(15)	–	–
586092A	08:32:08.70	-43:13:45.44	0.92	75	5.1±1.1(15)	1.5±0.3(15)	8.0±4.5(17)	<1.0(16)	<3.6(15)	<9.4(-3)	–
586092B	08:32:08.48	-43:13:49.28	0.92	150	<2.9(15)	<1.6(15)	0.1–2.1(17)	<5.6(15)	<4.3(15)	–	–
586092C	08:32:09.06	-43:13:43.28	0.92	150	<2.8(15)	<1.7(15)	<2.5(15)	<7.6(15)	<4.8(15)	–	–
615590 C1	09:24:41.96	-52:02:08.04	0.64	200	2.0±0.5(16)	<5.0(15)	1.4±0.7(18)	3.0±1.5(16)	<1.0(16)	7.1±5.2(-3)	<6.7(-1)
615590 C2	09:24:41.96	-52:02:08.04	0.64	150	1.5±0.3(16)	<5.0(15)	1.1±0.6(18)	<1.0(16)	<1.0(16)	<6.7(-3)	–
640076A	10:20:15.66	-58:03:56.32	0.87	150	<4.1(15)	<1.2(15)	0.1–2.9(17)	<4.3(15)	<5.3(15)	–	–
640076B	10:20:15.60	-58:03:53.47	0.87	150	<4.1(15)	<2.6(15)	0.1–2.9(17)	<3.0(15)	<6.7(15)	–	–
644284A	10:31:29.78	-58:02:19.27	0.86	150	6.2±1.4(15)	1.5±0.3(15)	4.2±2.2(17)	<4.0(15)	<3.8(15)	<6.7(-3)	–
644284B	10:31:29.63	-58:02:18.82	0.86	100	8.2±1.8(15)	1.5±0.3(15)	7.8±4.3(17)	<3.0(15)	<3.9(15)	<2.9(-3)	–
693050	12:35:35.05	-63:02:31.19	0.99	200	1.4±0.3(16)	3.1±0.7(15)	1.3±0.8(18)	1.1±0.3(16)	<3.0(15)	2.7±1.7(-3)	<3.9(-1)
695243	12:43:31.51	-62:36:13.25	0.98	150	<4.0(15)	<1.2(15)	<1.8(15)	<5.9(15)	<7.9(15)	–	–
704792	13:11:14.14	-62:45:06.80	1.29	150	<4.5(15)	<8.2(14)	<1.2(15)	<4.5(15)	<2.2(15)	–	–
705768	13:12:36.17	-62:33:34.43	0.87	150	9.3±2.2(15)	3.0±1.5(15)	1.3±0.8(18)	<6.3(15)	<4.9(15)	<3.7(-3)	–
706733A	13:14:22.78	-62:45:59.48	0.87	150	<2.7(15)	<1.8(15)	0.2–16.4(16)	<4.8(15)	<2.9(15)	–	–
706733B	13:14:22.99	-62:45:54.35	0.87	150	<6.7(15)	<1.5(15)	<2.0(15)	<6.6(15)	<2.9(15)	–	–
706733C	13:14:23.07	-62:45:47.54	0.87	150	<5.6(15)	<1.8(15)	<2.5(15)	<4.9(15)	<9.0(15)	–	–
706785A	13:14:26.92	-62:44:29.72	0.88	150	<3.2(15)	<2.1(15)	0.1–1.9(17)	<6.2(15)	<2.6(15)	–	–
706785B	13:14:26.55	-62:44:31.80	0.88	150	<3.3(15)	<2.9(15)	0.0–2.0(17)	<6.0(15)	<3.6(15)	–	–

Table B.1. continued.

Source	RA (J2000)	Dec (J2000)	θ_{beam} "	T_{ex} K	$N_{\text{H}_2\text{CH}_3\text{OH}}$ cm^{-2}	$N_{\text{CH}_3^{18}\text{OH}}$ cm^{-2}	$N_{\text{CH}_3\text{OH}}$ cm^{-2}	$N_{\text{CH}_2\text{DOH}}$ cm^{-2}	$N_{\text{CHD}_2\text{OH}}$ cm^{-2}	(D/H) $_{\text{CH}_3\text{OH}}$ ¹	(D/H) $_{\text{CH}_2\text{DOH}}$ ²
706785C	13:14:26.38	-62:44:30.24	0.88	150	<2.7(15)	<1.3(15)	<1.7(15)	<5.9(15)	<9.0(15)	–	–
706785D	13:14:25.64	-62:44:30.36	0.88	150	<4.4(15)	<3.2(15)	0.1–2.7(17)	<6.1(15)	<3.7(15)	–	–
707948	13:16:43.19	-62:58:32.83	0.88	150	1.8±0.4(17)	1.5±0.3(16)	1.1±0.6(19)	2.0±1.0(17)	6.5±4.8(16)	6.0±4.3(-3)	3.2±2.9(-1)
717461A	13:43:01.68	-62:08:51.42	1.29	150	7.6±1.9(15)	2.6±0.8(15)	1.1±0.4(18)	<3.7(15)	<2.5(15)	<2.0(-3)	–
717461B	13:43:01.74	-62:08:55.34	1.29	150	<2.2(15)	<1.9(15)	<2.8(15)	<3.8(15)	<3.6(15)	–	–
721992	13:51:58.27	-61:15:41.04	0.85	150	<4.4(15)	<1.9(15)	0.5–2.5(17)	<7.3(15)	<5.5(15)	–	–
724566	13:59:30.92	-61:48:38.27	0.83	150	2.9±0.6(16)	1.0±0.2(16)	4.0±2.3(18)	2.0±1.0(16)	<9.6(15)	1.7±1.3(-3)	<9.6(-1)
732038	14:13:15.05	-61:16:53.19	0.82	150	<7.6(15)	<4.8(15)	1.2–4.2(17)	<6.8(15)	<7.5(15)	–	–
744757A	14:45:26.35	-59:49:15.55	1.30	150	1.4±0.4(16)	4.1±0.9(15)	1.7±1.0(18)	8.0±4.0(15)	<2.5(15)	1.6±1.2(-3)	<6.3(-1)
744757B	14:45:26.16	-59:49:19.87	1.30	150	<1.9(15)	<4.1(15)	1.3–11.3(16)	<2.9(15)	<2.3(15)	–	–
759150A	15:10:43.13	-57:44:49.63	1.29	150	<1.9(15)	<1.2(15)	0.3–10.1(16)	<5.0(15)	<2.3(15)	–	–
759150B	15:10:43.52	-57:44:44.82	1.29	150	<2.4(15)	<9.6(14)	<1.5(15)	<5.0(15)	<2.8(15)	–	–
759150C	15:10:44.48	-57:44:47.33	1.29	150	<2.2(15)	<9.6(14)	<8.6(14)	<5.0(15)	<2.3(15)	–	–
759150D	15:10:42.71	-57:44:52.85	1.29	150	<5.0(15)	<9.7(14)	<1.2(15)	<4.9(15)	<2.3(15)	–	–
759150E	15:10:44.10	-57:44:52.03	1.29	150	<2.1(15)	<9.6(14)	<9.9(14)	<4.8(15)	<2.3(15)	–	–
767784	15:29:19.31	-56:31:22.02	1.29	100	3.9±0.5(16)	7.2±1.6(15)	2.5±1.4(18)	1.0±0.4(16)	<3.3(15)	1.4±1.0(-3)	<5.3(-1)
800287	16:11:26.57	-51:41:57.14	0.80	100	1.5±0.3(16)	6.2±1.4(15)	1.8±1.1(18)	1.0±0.5(16)	<1.3(16)	1.9±1.5(-3)	<2.7(0)
854214A	16:52:32.74	-43:23:49.60	1.26	150	<2.2(15)	<1.7(15)	0.7–9.5(16)	<3.8(15)	<5.0(15)	–	–
854214B	16:52:33.02	-43:23:50.26	1.26	150	<5.0(15)	<7.8(14)	0.1–2.1(17)	<3.8(15)	<2.7(15)	–	–
863312A	17:02:08.36	-41:46:56.89	0.83	150	<8.9(15)	<3.7(15)	<3.8(15)	<2.0(16)	<1.4(16)	–	–
863312B	17:02:09.14	-41:46:45.04	0.83	150	<3.7(15)	<1.9(15)	<2.0(15)	<6.0(15)	<4.2(15)	–	–
865468A C1	17:05:10.90	-41:29:06.99	1.23	100	1.3±0.3(17)	3.1±0.7(16)	1.0±0.6(19)	1.5±0.8(17)	4.0±2.0(16)	4.9±3.8(-3)	2.7±1.9(-1)
865468A C2	17:05:10.90	-41:29:06.99	1.23	150	5.1±1.1(16)	<3.0(15)	2.5±1.4(18)	6.0±3.0(16)	<2.0(16)	7.9±5.7(-3)	<6.7(-1)
865468B	17:05:11.22	-41:29:07.65	1.24	150	1.3±0.2(16)	2.6±0.6(15)	8.6±5.0(17)	6.5±2.0(15)	<5.0(15)	2.5±1.7(-3)	<1.1(0)
865468C	17:05:11.12	-41:29:03.47	1.24	150	5.0±1.9(15)	1.0±0.2(15)	3.4±2.0(17)	<7.5(15)	<5.8(15)	<1.8(-2)	–
876288	17:11:51.02	-39:09:29.18	0.81	150	8.9±2.9(15)	3.1±0.7(15)	5.7±3.9(17)	<6.0(15)	<5.0(15)	<1.2(-2)	–
881427A	17:20:06.31	-38:57:15.18	1.23	150	9.3±1.8(16)	2.6±0.7(16)	1.1±0.4(19)	8.3±1.6(16)	1.9±0.7(16)	2.5±1.1(-3)	2.3±1.0(-1)
881427B	17:20:06.46	-38:57:11.44	1.23	300	1.0±0.2(16)	8.2±1.8(15)	3.4±1.9(18)	1.5±0.8(16)	<1.0(16)	1.5±1.1(-3)	<1.3(0)
881427C	17:20:06.12	-38:57:15.84	1.23	150	7.4±1.6(16)	2.6±0.5(16)	1.1±0.4(19)	5.5±1.2(16)	1.2±0.5(16)	1.7±0.7(-3)	2.2±0.9(-1)
G023.3891+00.1851	18:33:14.32	-08:23:57.82	1.24	200	7.9±2.2(15)	2.5±1.2(15)	7.9±4.5(17)	9.5±3.0(15)	<5.0(15)	4.0±2.6(-3)	<7.6(-1)
G023.6566-00.1273	18:34:51.57	-08:18:21.81	1.24	150	1.4±0.4(16)	<5.0(15)	7.1±2.5(17)	2.5±1.2(16)	<5.0(15)	1.2±0.7(-2)	<4.0(-1)
G025.6498+01.0491	18:34:20.92	-05:59:42.08	1.17	150	3.0±0.6(16)	8.5±2.7(15)	3.4±1.4(18)	1.5±0.8(16)	5.0±2.5(15)	1.5±1.0(-3)	3.3±2.4(-1)
G030.1981-00.1691	18:47:03.05	-02:30:36.30	0.60	150	5.1±1.1(15)	<1.8(15)	2.2±1.2(17)	<1.5(16)	<1.6(16)	<4.7(-2)	–
G233.8306-00.1803	07:30:16.73	-18:35:49.06	0.81	150	<3.7(15)	<3.0(15)	<2.6(15)	<6.5(15)	<4.4(15)	–	–
G305.2017+00.2072A1	13:11:10.45	-62:34:38.60	1.30	150	1.2±0.3(16)	2.0±0.5(15)	8.5±4.8(17)	5.0±2.5(15)	<2.3(15)	2.0±1.5(-3)	<9.1(-1)
G305.2017+00.2072A2	13:11:13.12	-62:34:42.74	1.30	150	<8.8(15)	<5.0(15)	0.1–5.3(17)	<8.0(15)	<1.2(16)	–	–
G310.0135+00.3892	13:51:37.88	-61:39:07.74	1.30	150	<2.3(15)	<2.6(15)	0.3–13.5(16)	<7.9(15)	<2.9(15)	–	–
G314.3197+00.1125	14:26:26.25	-60:38:31.26	1.30	150	<2.4(15)	<2.2(15)	0.8–1.4(17)	<1.0(16)	<6.0(15)	–	–
G316.6412-00.0867	14:44:18.35	-59:55:11.28	1.29	100 ³	2.8±0.4(16)	8.6±2.7(15)	3.5±1.5(18)	2.8±0.5(16)	4.8±3.0(15)	2.7±1.2(-3)	1.7±1.1(-1)
G318.0489+00.0854B	14:53:42.64	-58:08:53.02	1.30	150	1.7±0.3(16)	4.9±1.9(15)	1.9±0.9(18)	8.0±4.0(15)	<3.0(15)	1.4±1.0(-3)	<7.5(-1)
G318.9480-00.1969A1	15:00:55.28	-58:58:52.60	1.29	100 ³	8.5±1.2(16)	2.2±0.4(16)	9.6±3.2(18)	7.0±1.1(16)	1.4±0.7(16)	2.4±0.9(-3)	2.0±1.1(-1)
G318.9480-00.1969A2	15:00:55.23	-58:58:55.88	1.29	150	<2.6(15)	<7.8(14)	0.4–16.0(16)	<6.5(15)	<2.3(15)	–	–
G323.7399-00.2617B1	15:31:45.64	-56:30:50.16	1.28	150	8.7±2.0(15)	2.0±0.5(15)	7.5±4.3(17)	<2.8(15)	<3.0(15)	<2.9(-3)	–

Table B.1. continued.

Source	RA (J2000)	Dec (J2000)	θ_{beam} "	T_{ex} K	$N_{\text{H}^{13}\text{CH}_3\text{OH}}$ cm^{-2}	$N_{\text{CH}_3^{18}\text{OH}}$ cm^{-2}	$N_{\text{CH}_3\text{OH}}$ cm^{-2}	$N_{\text{CH}_3\text{DOH}}$ cm^{-2}	$N_{\text{CHD}_2\text{OH}}$ cm^{-2}	(D/H) $_{\text{CH}_3\text{OH}}^{(1)}$	(D/H) $_{\text{CH}_3\text{DOH}}^{(2)}$
G323.7399-00.2617B2	15:31:45.45	-56:30:49.84	1.28	125	$8.2 \pm 1.8(16)$	$1.5 \pm 0.3(16)$	$5.7 \pm 3.3(18)$	$2.0 \pm 1.0(16)$	$4.0 \pm 2.0(15)$	$1.2 \pm 0.9(-3)$	$2.0 \pm 1.4(-1)$
G323.7399-00.2617B3	15:31:45.73	-56:30:51.93	1.28	150	$<2.5(15)$	$<6.0(14)$	$1.4-13.4(16)$	$<4.7(15)$	$<2.3(15)$	–	–
G323.7399-00.2617B4	15:31:45.94	-56:30:51.34	1.28	150	$<2.6(15)$	$<6.9(14)$	$1.2-14.2(16)$	$<2.7(15)$	$<2.8(15)$	–	–
G323.7399-00.2617B5	15:31:45.62	-56:30:45.62	1.28	150	$<2.6(15)$	$<5.8(14)$	$0.1-13.9(16)$	$<5.0(15)$	$<2.7(15)$	–	–
G323.7399-00.2617B6	15:31:45.84	-56:30:47.68	1.28	150	$<3.9(15)$	$<1.2(15)$	$0.1-2.1(17)$	$<2.6(15)$	$<3.7(15)$	–	–
G323.7399-00.2617B7	15:31:45.91	-56:30:46.10	1.28	150	$<1.7(15)$	$<1.2(15)$	$0.1-9.3(16)$	$<3.9(15)$	$<1.6(15)$	–	–
G327.1192+00.5103	15:47:32.72	-53:52:38.60	0.81	100	$4.0 \pm 0.9(16)$	$9.2 \pm 2.0(15)$	$2.9 \pm 1.7(18)$	$3.5 \pm 1.8(16)$	$<5.0(15)$	$4.0 \pm 3.1(-3)$	$<2.9(-1)$
G343.1261-00.0623	16:58:17.22	-42:52:07.54	1.25	100	$8.8 \pm 2.7(15)$	$<7.0(15)$	$5.0 \pm 1.8(17)$	$<4.0(16)$	$4.0 \pm 2.0(15)$	$<4.1(-2)$	$>5.0(-2)$
G345.5043+00.3480 C1	17:04:22.89	-40:44:23.06	1.25	125	$5.1 \pm 1.1(16)$	$1.0 \pm 0.2(16)$	$4.0 \pm 2.3(18)$	$5.0 \pm 2.5(16)$	$1.0 \pm 0.5(16)$	$4.2 \pm 3.2(-3)$	$2.0 \pm 1.4(-1)$
G345.5043+00.3480 C2	17:04:22.89	-40:44:23.06	1.25	150	$3.1 \pm 0.7(16)$	$<1.0(16)$	$1.7 \pm 0.9(18)$	$3.0 \pm 1.5(16)$	$<1.0(16)$	$5.9 \pm 4.3(-3)$	$<6.7(-1)$
G348.7342-01.0359B1	17:20:07.08	-38:57:11.22	1.23	150	$<3.4(15)$	$<9.9(14)$	$1.3-17.7(16)$	$<1.2(16)$	$<3.9(15)$	–	–
G348.7342-01.0359B2	17:20:07.26	-38:57:09.82	1.23	150	$<2.3(15)$	$<1.7(15)$	$0.1-11.9(16)$	$<3.6(15)$	$<4.1(15)$	–	–
G348.7342-01.0359B3	17:20:07.38	-38:57:10.15	1.23	150	$<4.0(15)$	$<1.5(15)$	$<1.4(15)$	$<1.1(16)$	$<3.8(15)$	–	–

Notes. The coordinates mark the position from which the spectra were extracted. All column densities are derived for the reported T_{ex} and assuming the source size is equal to the size of the beam (i.e., beam dilution = 1). The column density of CH_3OH is derived from the $\text{CH}_3^{18}\text{OH}$ and $^{13}\text{CH}_3\text{OH}$ isotopologues when these are detected. If neither isotopologue is detected but CH_3OH is, a range in column densities is presented where the lower limit is the column density derived from CH_3OH and the upper limit is scaled from the upper limit on $^{13}\text{CH}_3\text{OH}$. If CH_3OH itself is also not detected, an upper limit is directly derived from its spectrum.

⁽¹⁾ Derived from $N_{\text{CH}_3\text{DOH}}$ using Eq. (2). ⁽²⁾ Derived from $N_{\text{CHD}_2\text{OH}}$ using Eq. (3). ⁽³⁾ T_{ex} is set to 150 K for deuterated isotopologues and to 100 K for the other isotopologues.

Appendix C: Methanol D/H ratios of sources in the literature

Table C.1. The $(D/H)_{CH_3OH}$ and $(D/H)_{CH_2DOH}$ ratios taken from the literature that are included in Figs. 3 and 4.

Source	Type ⁽¹⁾	$(D/H)_{CH_3OH}$	$(D/H)_{CH_2DOH}$	Refs
B1-c	LMP	$2.8 \pm 0.9(-2)$	$1.3 \pm 0.2(-1)$	1,2
Serpens S68N	LMP	$1.4 \pm 0.6(-2)$	$1.2 \pm 0.5(-1)$	1,2
B1-bS	LMP	$<1.8(-2)$	–	1,2
HH212	LMP	$3.8 \pm 2.3(-2)$	–	3
		$8.1 \pm 3.0(-3)$	–	4
IRAS 16293A	LMP	$2.8 \pm 1.2(-2)$	$2.0 \pm 0.7(-1)$	5,6
IRAS 16293B	LMP	$2.4 \pm 0.9(-2)$	$2.5 \pm 0.9(-1)$	6,7
IRAS 2A	LMP	$1.9 \pm 1.0(-2)$	$7.0 \pm 2.6(-1)$	8
IRAS 4A	LMP	$1.4 \pm 0.8(-2)$	$5.6 \pm 2.2(-1)$	8
L483	LMP	$7.8 \pm 3.3(-3)$	–	9
BHR71	LMP	$9.6 \pm 4.1(-3)$	–	10
Ser-emb 1	LMP	$<2.0(-1)$	–	11
Ser-emb 11W	LMP	$<4.3(-2)$	–	12
HOPS-108	LMP	$7.0 \pm 3.8(-3)$	–	13
G192.12–11.10	LMP	$9.8 \pm 5.8(-3)$	–	14
G205.46–14.56S1–A	LMP	$6.7 \pm 3.3(-3)$	–	14
G208.68–19.20N1	LMP	$1.3 \pm 0.6(-2)$	–	14
G210.49–19.79W–A	LMP	$1.4 \pm 0.6(-2)$	–	14
G211.47–19.27S	LMP	$1.7 \pm 0.4(-2)$	–	14
V883 Ori	LMP	$4.8 \pm 1.0(-2)$	–	15
Serpens SMM1-a	IMP	$3.6 \pm 2.1(-3)$	–	16
NGC 7192 FIRS2	IMP	$1.9 \pm 0.8(-3)$	–	17
Cep E-A	IMP	$1.2 \pm 0.4(-2)$	–	18
Sgr B2(N2)	HMP	$4.0 \pm 1.7(-4)$	–	19,20
NGC6334I MM1 I	HMP	$3.0 \pm 1.7(-4)$	–	21
NGC6334I MM1 II	HMP	$1.8 \pm 0.9(-4)$	–	21
NGC6334I MM1 III	HMP	$3.2 \pm 1.8(-4)$	–	21
NGC6334I MM1 IV	HMP	$1.6 \pm 1.0(-4)$	–	21
NGC6334I MM1 V	HMP	$2.3 \pm 1.1(-4)$	–	21
NGC6334I MM2 I	HMP	$6.0 \pm 3.6(-4)$	–	21
NGC6334I MM2 II	HMP	$1.5 \pm 0.7(-4)$	–	21
NGC6334I MM3 I	HMP	$2.4 \pm 1.1(-4)$	–	21
NGC6334I MM3 II	HMP	$2.6 \pm 1.1(-4)$	–	21
Orion KL ridge	HMP	$1.7 \pm 0.7(-3)$	–	22
Orion KL HC	HMP	$<1.7(-3)$	–	22
CygX-N30	HMP	$<1.7(-3)$	–	23
L1495-B10 6	LMPC	$1.4 \pm 0.4(-2)$	–	24
L1495-B10 7	LMPC	$4.8 \pm 1.3(-2)$	–	24
L1495-B10 8	LMPC	$5.2 \pm 1.5(-2)$	–	24
L1495-B10 9	LMPC	$4.6 \pm 1.1(-2)$	–	24
L1495-B10 10	LMPC	$4.2 \pm 1.3(-2)$	–	24
L1495-B10 11	LMPC	$<1.9(-2)$	–	24
L1495-B10 12	LMPC	$2.0 \pm 0.4(-2)$	–	24
L1495-B10 13	LMPC	$<3.5(-2)$	–	24
L1495-B10 14	LMPC	$<1.4(-2)$	–	24
L1495-B10 15	LMPC	$4.0 \pm 1.1(-2)$	–	24
L1495-B10 16	LMPC	$3.0 \pm 1.0(-2)$	–	24
L1495-B10 17	LMPC	$8.8 \pm 2.7(-2)$	–	24
L183	LMPC	$1.3 \pm 0.2(-2)$	–	25
L1544	LMPC	$3.0 \pm 1.3(-2)$	–	26
I00117-MM2	HMSC	$<2.4(-3)$	–	27
AFGL 5142-EC	HMSC	$9.0 \pm 3.8(-4)$	–	27
05458-mm3	HMSC	$2.3 \pm 1.0(-3)$	–	27
G034-G2(MM2)	HMSC	$1.4 \pm 0.6(-2)$	–	27
G034-F2(MM7)	HMSC	$<2.5(-3)$	–	27
G034-F1(MM8)	HMSC	$<1.5(-3)$	–	27

Table C.1. continued.

Source	Type ⁽¹⁾	(D/H) _{CH₃OH}	(D/H) _{CH₂DOH}	Refs
G034-C1(MM9)	HMSC	<8.7(-4)	–	27
I20293-WC	HMSC	<1.9(-3)	–	27
I22134-G	HMSC	<1.7(-3)	–	27
I22134-B	HMSC	<6.7(-3)	–	27

Notes. The (D/H)_{CH₃OH} and (D/H)_{CH₂DOH} ratios are either directly taken from the reported literature or computed using Eqs. (2) and (3) using the column densities from the reported literature. A 30% uncertainty was assumed in cases where no uncertainty was reported.

⁽¹⁾ LMP: low-mass protostar, IMS: intermediate-mass protostar, HMS: high-mass protostar, LMPC: low-mass prestellar core, HMSC: high-mass starless core.

References. 1: van Gelder et al. (2020); 2: Appendix D; 3: Lee et al. (2019a); 4: Bianchi et al. (2017b); 5: Manigand et al. (2020); 6: Drozdovskaya et al. (2022); 7: Jørgensen et al. (2018); 8: Taquet et al. (2019); 9: Jacobsen et al. (2019); 10: Yang et al. (2020); 11: Martín-Doménech et al. (2019); 12: Martín-Doménech et al. (2021); 13: Chahine et al. (2022); 14: Hsu et al. (2022); 15: Lee et al. (2019b); 16: Ligterink et al. (2021); 17: Fuente et al. (2014); 18: Ospina-Zamudio et al. (2018); 19: Bellocche et al. (2016); 20: Müller et al. (2016); 21: Bøgelund et al. (2018); 22: Neill et al. (2013); 23: van der Walt et al. (2021); 24: Ambrose et al. (2021); 25: Lattanzi et al. (2020); 26: Bizzocchi et al. (2014); 27: Fontani et al. (2015).

Appendix D: Doubly deuterated methanol in B1-c, Serpens S68N, and B1-bS

Using the database entry of CHD₂OH provided by Drozdovskaya et al. (2022), transitions from CHD₂OH can also be searched for in a few COM-rich low-mass protostars. Here, this is done for B1-c, Serpens S68N (hereafter S68N), and B1-bS from the 2017.1.01174.S ALMA program. The content of oxygen-bearing COMs for these sources was presented by van Gelder et al. (2020), but no public database entry was yet available for CHD₂OH at that time.

Only one strong transition of CHD₂OH ($7_{1,2}0_1 - 7_{0,1}0_0$, $E_{\text{up}} = 68$ K) is available for these sources which lies on the very edge of the covered frequency range. For B1-c and S68N, this transition is detected at the 3σ level, but given that only half the line is observed this detection is still tentative. Using the same method for deriving the column densities as used by van Gelder et al. (2020) and assuming an excitation temperature of 150 K, we derive column densities of $2.0 \pm 0.6 \times 10^{16} \text{ cm}^{-2}$ for B1-c, $7.2 \pm 2.7 \times 10^{15} \text{ cm}^{-2}$ for S68N, and $< 1.7 \times 10^{15} \text{ cm}^{-2}$ for B1-bS. The FWHM was fixed to the average FWHM of those sources of 3.2 km s^{-1} , 5.5 km s^{-1} , and 1.0 km s^{-1} , respectively (van Gelder et al. 2020). The resulting fits are shown in Fig. D.1. Using these derived column densities and those reported for CH₃OH by van Gelder et al. (2020), the (D/H)_{CH₂DOH} ratios for B1-c and S68N (for B1-bS, both CH₂DOH and CHD₂OH are not detected) are shown in Fig. 4 and agree very well with those derived for other low-mass sources as well as with the high-mass sources.

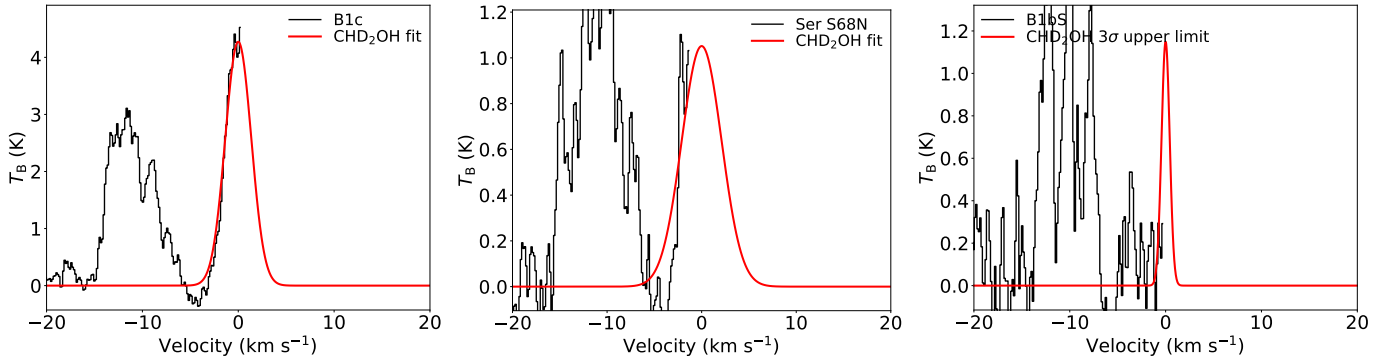


Fig. D.1. Spectral line fits of CHD₂OH $7_{1,2}0_1 - 7_{0,1}0_0$ ($E_{\text{up}} = 68$ K) line for B1-c (left), Serpens S68N (middle), and B1-bS (right). The data corrected for the V_{lsr} are shown in black and the best fit for $T_{\text{ex}} = 150$ K is shown in red.

Appendix E: Additional figures

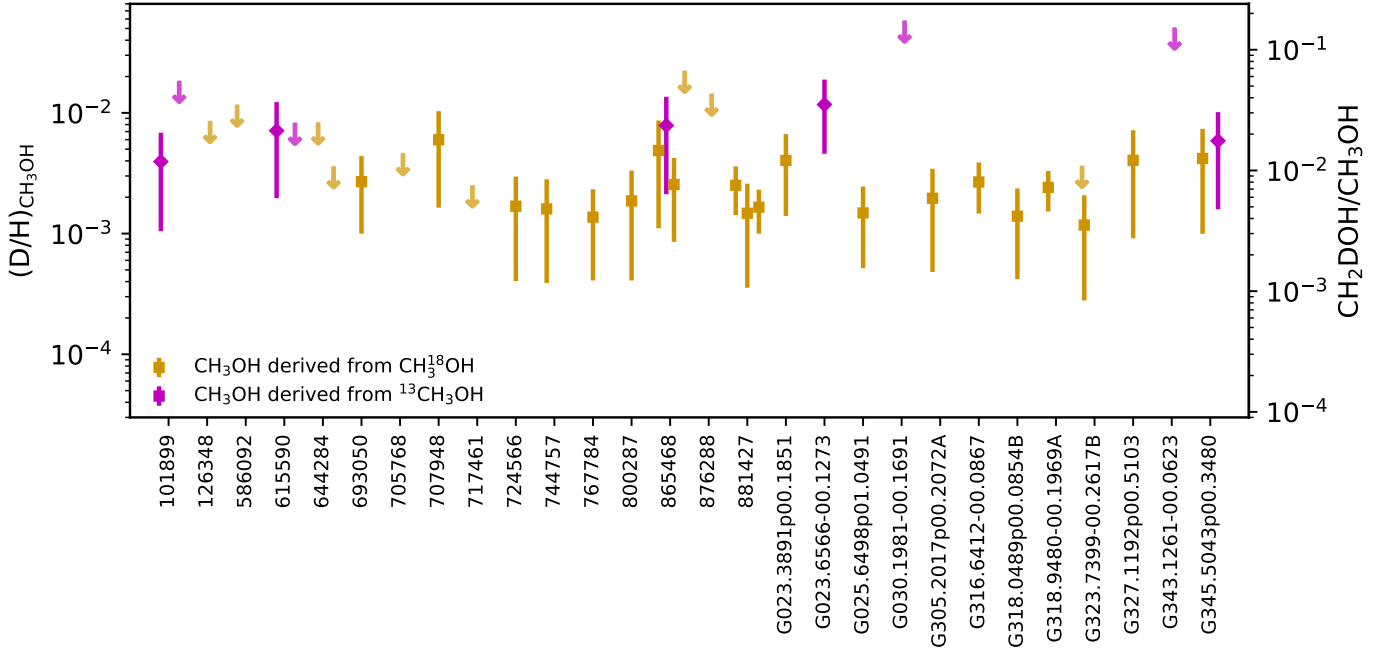


Fig. E.1. The $(D/H)_{CH_3OH}$ ratios derived from the N_{CH_2DOH}/N_{CH_3OH} ratios for the ALMAGAL sources presented in this work, indicating whether N_{CH_3OH} was derived from the ^{13}C isotopologue (magenta diamonds) or from the ^{18}O isotopologue (orange squares). Upper limits are presented as arrows.

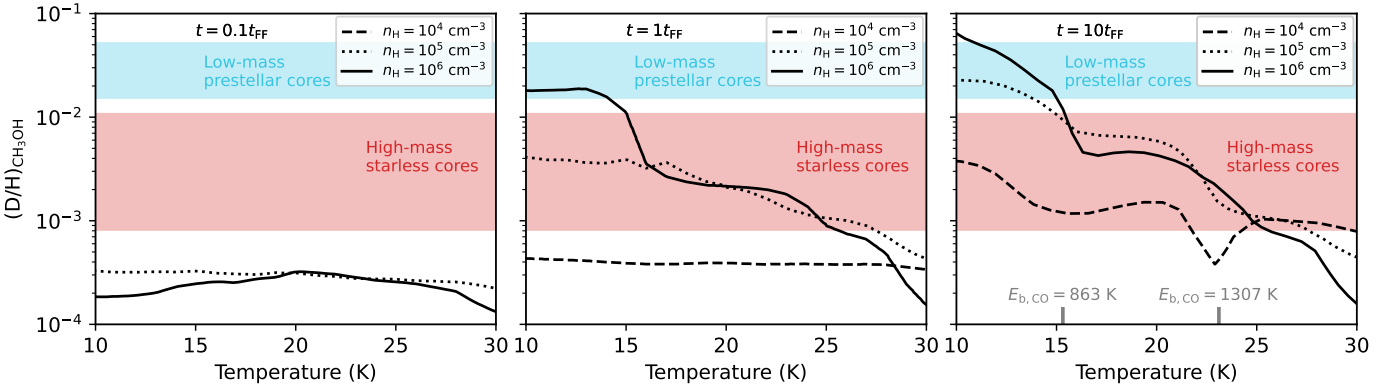


Fig. E.2. Same as Fig. 6 but now showing the average measured $(D/H)_{CH_3OH}$ for low-mass prestellar cores (light blue) and high-mass starless cores (red).